Investigation of observational error sources in multi Doppler radar three-dimensional variational vertical air motion retrievals

Mariko Oue[1], Pavlos Kollias[1,2,3], Alan Shapiro[4], Aleksandra Tatarevic[3], Toshihisa Matsui[5]

[1]School of Marine and Atmospheric Sciences, Stony Brook University, Stony Brook, 11794, USA
5   [2]Environmental and Climate Sciences Department, Brookhaven National Laboratory, Upton, 11973, USA
[3]Department of Atmospheric and Oceanic Sciences, McGill University, Montreal, H3A 0G4, Canada
[4]School of Meteorology, University of Oklahoma, Norman, 73019, USA
[5] Mesoscale Atmospheric Processes Laboratory NASA Goddard Space Flight Center, Greenbelt, 20771, USA

10   *Correspondence to*: Mariko Oue (mariko.oue@stonybrook.edu)

Abstract. Multi-Doppler radar network observations have been used in different configurations over the last several decades to conduct three-dimensional wind retrievals in mesoscale convective systems. Here, the impacts of the selected radar volume coverage pattern (VCP), the sampling time for the VCP, the number of radars used, and the added value of advection correction on the retrieval of the vertical air
15   motion in the upper part of convective clouds are examined using the Weather Research and Forecasting (WRF) model simulation, the Cloud Resolving Model Radar SIMulator (CR-SIM), and a three-dimensional variational multi-Doppler radar retrieval technique. Comparisons between the model truth (i.e., WRF kinematic fields) and updraft properties (updraft fraction, updraft magnitude, and mass flux) retrieved from the CR-SIM-generated multi-Doppler radar field are used to investigate these impacts. The
20   findings are: 1) the VCP elevation strategy and sampling time have a significant effect on the retrieved updraft properties above 6 km altitude; 2) 2-min or shorter VCPs have small impacts on the retrievals, and the errors are comparable to retrievals using a snapshot cloud field; 3) increasing the density of elevations angles in VCP appears to be more effective to reduce the uncertainty than an addition of data from one more radar, if the VCP is performed in 2 minutes; and 4) the use of dense elevation angles
25   combined with an advection correction applied to the 2-min VCPs can effectively improve the updraft retrievals, but for longer VCP sampling periods (5 min) the value of advection correction is challenging. This study highlights several limiting factors in the retrieval of upper-level vertical velocity from multi-Doppler radar networks and suggests that the use of rapid-scan radars can substantially improve the quality of wind retrievals if conducted in a limited spatial domain.

1 Introduction

Measurements of vertical air motion in deep convective clouds are critical for our understanding of the dynamics and microphysics of convective clouds (e.g., Jorgensen and LeMone, 1989). Convective mass flux is responsible for the transport of energy, mass and aerosols in the troposphere, which significantly impact large-scale atmospheric circulation and local environment and affect the probability of subsequent formation of clouds (e.g., Hartmann et al., 1984; Su et al., 2014; Sherwood et al., 2014). Consequently, the vertical air motion estimates are widely employed to improve convective parameterizations in global model (e.g., Donner et al., 2001) and also to evaluate the cloud resolving model (CRM) simulations and large eddy simulations (LES, e.g. Varble et al., 2014; Fan et al., 2017).

Aircraft penetration of convective clouds offer the most direct method to measure the vertical air motions (e.g. Lenschow, 1976); however, practical hazards and operational costs have resulted in a valuable but limited dataset (e.g., Byers and Braham, 1948; LeMone and Zipser, 1980). Current aviation regulation does not permit such penetration anymore. Ground-based and airborne profiling Doppler radars provide a high degree of detail of convective clouds in both time and height and can sample even the most intense convective cores (e.g., Wakasugi et al., 1986; Heymsfield et al., 2010; Williams, 2012; Giangrande et al., 2013; Kumar et al., 2015). One drawback of profiling radar techniques is their limited sampling of individual storms and the lack of information on the temporal evolution of the convective dynamics and structure; the observational limitations, thus, make the use of the techniques in model evaluation challenging.

Since the pioneering work of Lhermitte and Miller (1970), networks of two or more scanning Doppler radars and the use of multi-Doppler radar wind retrieval techniques have been widely used to overcome the aforementioned limitations (Junyent et al., 2010; North et al., 2017). In addition to research radars, operational Doppler radar networks can, in certain conditions, accomplish a large coverage of multi-Doppler radar retrievals (e.g., Bousquet et al., 2007; Dolan and Rutledge, 2007, Park and Lee, 2009). While various Doppler radar wind retrieval techniques have been proposed (Chong and Testud, 1996; Chong and Campos, 1996; Bousquet and Chong, 1998; Gao et al., 1999; Protat and Zawadzki, 1999; Bell et al., 2012), three-dimensional variational (3DVAR) techniques are commonly used because of their robust and reliable solutions by minimizing errors (e.g., Potvin et al., 2012b).

Multi-Doppler radar analysis have been used to better understand mesoscale dynamics, low-level divergence, and microphysical-dynamical interactions (e.g., Kingsmill and House, 1999; Friedrich and Hagen, 2004; Stonitsch and Markowski, 2007; Collis et al., 2013; Oue et al., 2013, and many others). There is also considerable literature discussing different sources of uncertainties in dual- or multi-Doppler radar wind retrieval. The interpolation and smoothing techniques used (Cressman, 1959; Barnes, 1964, Given and Ray, 1994; Miller and Fredrick, 1998) can have an impact on the quality of Doppler radar wind retrieval (e.g., Collis et al., 2010). Another source of uncertainties is related to the hydrometeor fall speed estimates (e.g., Steiner, 1991; Caya, 2001), especially at shorter wavelengths (e.g., X and C bands) where the signal attenuation can bias the estimates. Clark et al. (1980) estimated errors attributed to cloud evolution in horizontal and vertical wind estimates from multiple Doppler radar measurements. Bousquet et al. (2008) estimated uncertainties in wind fields from their operational multi-Doppler radar retrieval, by simulating radar measurements using numerical model output. They pointed out that missing low-level measurements and poor vertical sampling could produce significant uncertainties in retrieval of low-level wind fields. These investigations have been conducted by formulating suitable Observing System Simulation Experiments (OSSEs). Potvin et al. (2012b) investigated potential sources of errors in multi-Doppler radar wind retrievals for supercell observations using OSSEs. They suggested that the magnitudes of vorticity and its tendency fields were sensitive to the smoothness constraint in the analysis, and assumptions of spatially constant storm motion and no storm-evolution led to significant errors in middle and upper levels.

A common result from the studies above is that the uncertainties increase with height because scanning radar data density inevitably becomes lower at higher altitudes. Meanwhile, deep convective clouds generally show maximum updrafts at middle and upper parts of the clouds (e.g., Giangrande et al., 2013). Here we are concerned with the retrieval uncertainties of vertical air motion especially in the middle and upper levels of deep convective clouds. The motivation for this study is two-fold. First, the US Department of Energy (DOE) Atmospheric Radiation Measurement (ARM) program operates an atmospheric observatory at Southern Great Plains (SGP), Oklahoma (Mather and Voyles, 2013), where scanning Doppler radars and profiling instruments provide unique dynamical and microphysical measurements. During the Midlatitude Continental Convective Clouds Experiment (MC3E, Jensen et al.,

2016), the ARM precipitation scanning Doppler radars accomplished dense network of Doppler radar measurements of deep convective clouds explicitly designed to retrieve three-dimensional (3D) wind (North et al., 2017). However, our experience with the data and a series of experiments performed in this study suggest that despite the plethora of radar systems at the ARM SGP observatory, the 3D wind retrievals are subject to large errors especially at the upper levels. It is possible that some of the errors are associated with radar volume coverage pattern strategy that does not satisfy the requirement for high spatiotemporal observations. This issue has been highlighted in recent studies with high-resolution CRM simulations of convective cloud properties (e.g., Morrison et al., 2015; Hernández-Deckers and Sherwood, 2016). Secondly, the paucity of available datasets of vertical air motion limits our ability to quantitatively analyze structures and characteristics of the mesoscale convective systems (MCSs) and evaluate model outputs of the MCSs (e.g., Varble et al., 2014; Liu et al., 2015; Donner et al., 2016; Fan et al., 2017). Thus, we are interested in determining the sampling capabilities required for a multi-Doppler radar network to address these errors and investigating if radar networks based on different technology (e.g., phased-array radars, Otsuka et al., 2016; Kollias et al., 2018a) can address these errors. To do so, we focus on impact of the multi-Doppler radar network setup and not how we quality-control, interpolate or use the Doppler radar observations in a minimization routine. The latter is the same in all the experiments performed here and is described in North et al. (2017). We investigate the impact of the selected radar volume coverage pattern (VCP), the sampling time for the VCP, the number of radars used and the added value of advection correction upon the uncertainties of multi-Doppler radar wind retrieval.

2 Data and methodology

In this study, the OSSE is conducted for an MCS case on 20 May 2011 observed in Oklahoma during the MC3E. This squall-line MCS was oriented in northeast-southwest direction extending for approximately 1000 km (Fan et al., 2017). The convective region was approximately 50 km wide and trailed a distinct stratiform precipitation area when it passed through the ARM SGP site from 09:20 UTC to 11:40 UTC. This case has been analyzed for its dynamical and microphysical structures by several previous studies (e.g., Liu et al., 2015; Wu and McFarquhar, 2016; Fan et al., 2017).

OSSE studies are generally used to assess impacts of operational observing systems on, for example, observation-based value-added products and weather forecasts (Timmermans et al., 2009). The OSSE conducted in this study consists in:

1) Produce the set of simulation data by a high resolution numerical weather model of a convective cloud system and generate the model hydrometeor and dynamical fields at a high temporal resolution to capture the storm evolution at scales unresolved by typical VCPs;

2) Use a sophisticated radar simulator to reproduce the VCP of a multi-Doppler radar system and produce radar observables at radar coordinates with the realistic radar characteristics (beamwidth, range resolution and sensitivity);

3) Grid the simulated radar observations to a Cartesian coordinate and conduct a variational 3D multi-Doppler wind retrieval algorithm to estimate the dynamical field; and

4) Evaluate the retrieved wind field against the corresponding field from the numerical model direct output.

The Weather Research Forecasting model (WRF) is used to produce simulation of the MCS case on 20 May 2011 (step 1). The WRF output is used as an input to the Cloud Resolving Model Radar SIMulator (CR-SIM; Tatarevic et al., 2018) to simulate equivalent radar reflectivity factor (Z) and Doppler velocity (V_r) from scanning radars (step 2). The simulated Z and V_r fields are then resampled and converted into radar polar coordinate according to VCPs (step 2). The Z and V_r fields at radar polar coordinate are converted into the Cartesian grid, and then they are used to estimate 3D wind field using the 3DVAR multi-Doppler radar wind retrieval algorithm developed by North et al. (2017) (step 3). The obtained vertical velocity fields are compared against the WRF-simulated dynamical field to investigate impacts of the limitations attributed to the radar observations and the retrieval technique on the retrieved vertical wind field (step 4).

2.1   WRF Simulation for 20 May 2011 MCS

The WRF simulation horizontal domain is 960 km x 720 km with 0.5 km horizontal grid spacing. The vertical resolution varies from approximately 30 m near the surface to 260 m at 2 km altitude and maintains this resolution approximately constant above 2 km altitude. To include time evolution in

volume scan coverage pattern, the WRF simulation provides output every 20 seconds. The Morrison double moment microphysics scheme was used, which predicts mass and number mixing ratios for liquid cloud, rain, ice cloud, snow, and a medium density lump graupel representing the rimed ice with a switch to modify the settings for graupel to a high density hail (Morrison et al., 2005). Tao et al. (2016) pointed out that simulations including the hail option better represented the observed MCSs during the MC3E period than those not using hail. In their study for the May 20 MC3E case, Fridlind et al. (2017) used the Morrison double moment microphysics scheme with the hail option. The present study also applies the hail category to the simulation instead of graupel. The simulated MCS comprised a convective precipitation region at the leading edge of the system and a stratiform precipitation trailed by the convective region, as similar as the observation. The MCS passed through the ARM SGP radar observation site approximately one hour later than the observation (at around 12:18 UTC), and a stronger convective precipitation region formed slightly (~20 km) to the north of the ARM SGP site. In this study, we treat the WRF-simulated vertical velocity field as "truth" to evaluate the performance of multi-Doppler radar wind retrieval.

2.2   CR-SIM Simulation of 20 May 2011 MCS case

The CR-SIM is a sophisticated radar forward operator developed to bridge the gap between high-resolution cloud model output and radar observations (Tatarevic et al., 2018). The CR-SIM can be applied on the 3D model output produced by a variety of CRM and LES, such as WRF, Regional Atmospheric Modelling System (RAMS), System for Atmospheric Modelling (SAM), and the ICOsahedral Nonhydrostatic (ICON) model. It emulates the interaction between transmitted polarized radar waves and rotationally symmetric hydrometeors and can simulate the power (equivalent radar reflectivity factor), phase (Doppler velocity) and polarimetric (specific differential phase, differential reflectivity, depolarization) variables with a fixed elevation angle or varying elevation angles with respect to a specified radar location.

Several experiments are performed to evaluate the limitations of the sensing techniques employed in the network of three X-band Scanning ARM Precipitation Radars (X-SAPRs, named I4, I5, and I6, respectively) at the SGP site (Fig. 1), which provided high-resolution radar observations of convective

systems during the MC3E (e.g., North et al., 2017). The ARM SGP network is selected because it is comprised by three identical radar systems that are employed together and can be operated in a coordinated manner. Furthermore, since it is a long-term facility for the study of deep convective clouds, it is important to assess the capability and uncertainties. Using CR-SIM, we simulated measurements of the three X-SAPRs. In order to investigate the impact of an increased number of radars, observations from the C-band Scanning ARM Precipitation Radar (C-SAPR) at the SGP site (Fig. 1) are also simulated. Characteristics and settings of the simulated radar measurements are shown in Table 1. To investigate the impact of increasing the number of elevation angles and the maximum elevation angle, a VCP including additional elevation scans for the X-SAPR measurements is introduced. These simulations with X-SAPR aim to examine effects of using faster scanning radars, such as the Doppler on Wheels (DOW, Wurman, 2001), the Atmospheric Imaging Radar (AIR, Isom et al., 2013), the Rapid scanning X-band polarimetric (RaXPol, Pazmany et al., 2013) and low-power X-band phased array radars (LPAR, Kollias et al., 2018a). Locations of radars used in this study and the simulated retrieval domain are shown in Fig. 1. Details about the elevation angle settings are described in Sect. 2.4.

The retrieval simulation domain size is $50\,\text{km} \times 50\,\text{km} \times 10\,\text{km}$ above the ground level (AGL) centered around the ARM SGP Central Facility (CF). In the simulations, CF and the domain were virtually located within a vigorous convective region of the MCS to capture the intense vertical velocity (Fig 1b). We assume that the lowest boundary of the simulation domain is idealized as flat at the ground level of 0.3 km above sea level.

For each radar, the CR-SIM forward simulated Z and V_r are provided at the WRF grid coordinate by CR-SIM. They are then converted into radar polar coordinates considering all the radar characteristics that control the spatial resolution of radar observations (range weighting function, antenna beamwidth, and VCP strategy). The settings shown in Table 1 are consistent with the settings used during the MC3E period. For each radar the minimum detectable signal (Z_{min}) curve, which is attributed to the number of samples integrated for each radar sampling volume, is estimated using an equation $Z_{min}(r) = C + 20\log_{10}(r)$. In this equation, Z_{min} is expressed in logarithmic units (dBZ) with the range r (distance from the radar) in km, and the constant C that depends on the radar system characteristics expressed in dBZ; C

= -40 for X-band radars and C = -35 for C-band radar are used in this study. These values are similar to those for X-SAPRs and C-SAPR at the SGP site.

2.3   Wind Retrieval

The 3DVAR wind retrieval technique described in North et al. (2017) is used to estimate the 3D wind field. The wind retrieval algorithm inputs the Cartesian coordinate Z and V_r fields from each radar and uses a 3DVAR technique proposed by Potvin et al. (2012a). In the technique, the optimal wind field solution is obtained at the minimum of a cost function which consists of the physical constraints of radar radial velocity observations, anelastic mass continuity, surface impermeability, background wind field, and spatial smoothness. The surface impermeability constraint was used to dictate that vertical velocity vanishes at the ground with a relatively large weight. Details of the constraints are described in North et al. (2017).

The simulated Z and V_r with the radar polar coordinate are converted to the Cartesian coordinates for each radar measurement at horizontal and vertical spacings of 0.25 km using a single-pass isotropic Barnes distance-dependent weight (Barnes, 1964), with a constant smoothing parameter κ.

$$w_{i,q}(d) = \exp\left(\frac{-d^2}{\kappa}\right) \forall \; i = 1, \dots, n \text{ and } q = 1, \dots, Q \qquad (1)$$

Here $w_{i,q}$ is the weight for grid box i and radar gate q separated by distance d. The equation was applied in both horizontal and vertical interpolations. At each grid box, radar moments are estimated using the nearest 200 radar data gates with weights (Eq. 1) using κ = 0.13 km^2 for interpolation. The cutoff distance is determined as the distance where the weight is less than 0.01 (d ≈ 0.8 km). These parameters are chosen so that the statistical error in retrieved vertical velocity is minimal for the present case. Generally, data density at constant altitudes decreases with height and when increasing a distance from radar. Figures 2c-f show distance to the nearest radar data point at each Cartesian grid box at constant altitudes. These settings for gridding are fixed for all radar simulations, and this study does not consider uncertainties attributed to the settings for gridding process. The gridding technique has been well optimized in North et al. (2017), and the uncertainties in the gridding method and data smoothing processes have been well investigated in previous studies (e.g. Majcen et al., 2008; Potvin et al., 2012a).

There are several important sources of errors when considering the retrieval of vertical motion in convective systems other than the radar VCP; the most important among them are: unfolding of observed Doppler velocity, estimation of hydrometeor fall velocities, attenuation correction, and assumption of background environments. In all experiments in this study, Doppler velocity folding is disabled as an option, thus, the simulated radial Doppler velocities are correct and do not need to be unfolded. This eliminates the possibility of errors being introduced by incorrect Doppler velocity unfolding.

The difference between the "true" hydrometeor fall velocity V_f and the assumption based on an empirical formula that relates V_f with the radar reflectivity (e.g., Caya, 2001) can be a possible source of errors in wind retrievals (e.g., Potvin et al., 2012b; North et al., 2017). In the WRF simulations used here, V_f is parameterized depending on the microphysics scheme as a function of particle diameter. The hydrometeor's fall speeds (V_f) are given as a function of the hydrometeor diameter (D) and altitude (h) in a form:

$$V_f(h, D) = f_c(h) \cdot a_v \cdot D^{b_v} \tag{2}$$

where a_v and b_v are coefficients, and $f_c(h) = \left(\rho_{surf}/\rho(h)\right)^k$ is the correction factor for air density ($\rho(h)$: air density at height h, ρ_{surf}: surface air density) with exponent k (Morrison et al., 2005; Tatarevic et al., 2018). In the CR-SIM, reflectivity-weighed mean velocity is computed at each grid box in the following manner. The hydrometeor fall speeds as a function of the hydrometeor diameter are averaged over the diameter range with weights that are proportional to the CR-SIM estimated reflectivity for each hydrometeor particle size, and then the mean hydrometeor fall speeds are again averaged over all hydrometeor types present in each grid box with weights of reflectivity. In all experiments carried out in this study, the simulated reflectivity-weighted mean V_f are used in the retrieval, thus, no error attributed to the fall velocity estimates is introduced in the wind retrieval technique.

Another source of errors is the impact of signal attenuation by the hydrometeors along the propagation path, especially in C-band and X-band radar measurements. Since the attenuation is unknown, any attenuation-corrected radar reflectivity acts as a possible error source in the wind retrievals, particularly for hydrometeor fall speed estimates. However, as previously specified, the hydrometeor particle size

distributions and V_f used in this study are the ones prescribed by the WRF model microphysics, thus, no error is introduced.

Finally, the background horizontal wind vector, temperature, and air density are obtained by averaging WRF output values over the retrieval domain at each altitude and are used in place of sounding measurements over the SGP CF site. Although this study does not consider uncertainties in the background assumption, the change in the background data would have small impact on the retrieved updraft velocities as discussed in North et al. (2017).

2.4   Settings for wind retrieval experiments

Three factors influencing the updraft velocity estimates are investigated. The first is radar volume coverage pattern (VCP) which determines the set of elevation angles used by the radars to sample the volume of the analysis domain. The second is time interval needed by the radars of the network to complete the specified VCP to emulate both the advection and temporal evolution of the convective cloud system. Third, the added value of the advection correction for the different sets of VCP settings is evaluated. The experiments and their names are listed in Table 2.

2.4.1   Control wind retrieval simulation (3FullGrid)

The control wind retrieval simulation is an ideal, instantaneous VCP where all radars of the network sample all the WRF grid points. As a result, three measurements of equivalent radar reflectivity factor and radial Doppler velocity from the three X-SAPRs are available at each grid box of the WRF grid (named 3FullGrid). This experiment does not undergo the conversion process from the WRF grid to radar coordinate or the gridding process from radar coordinate to the Cartesian coordinates. Therefore, this does not include uncertainties from VCP, radar characteristics (beamwidth and range-bin spacing), or gridding process. Thus, the retrieved wind field should be a very good estimate of the true wind field and only the potential uncertainty in the wind retrieval algorithm can affect its quality. In this OSSE, the 3FullGrid is used for an upper bound of the performance of any of the conducted experiments and also serves as a sanity check for the wind retrieval algorithm.

2.4.2 Radar VCP

In a typical radar VCP, the number of elevation angles depends on the antenna scan rate and the desired time period for completing the VCP (typically 5-6 min). The antenna scan rate depends on the pedestal technical specifications and the minimum number of radar samples needed to estimate the radar observables with low uncertainty. The elevation angles are generally tightly selected at low elevations to provide good coverage over long horizontal distances and relatively sparse at higher elevations as the X-SAPR's VCP shown in Table 1 and Figure 1c.

In the experiments performed here, the impact of an increased number of elevation angles especially at high elevations is investigated while the antenna beamwidth, range-gate spacing, and maximum unambiguous range are kept unchanged and similar to the radar settings during MC3E. The following VCP are used: i) three X-SAPRs with the general VCP which is the same as during MC3E (named 3XR, Fig. 1c); ii) three X-SAPRs with denser elevation angles (named 3LR, Fig. 1d; the name "LR" stands for low-power X-band phased array radar, LPAR, Kollias et al., 2018a); and iii) same as i) but the C-SAPR measurements are added (named 4SR). Details of the VCPs are shown in Table 1. The settings i) and iii) use general VCPs for X-SAPR and C-SAPR which are the same as those during MC3E. The X-SAPR VCP is composed of 21 elevation angles ranging from 0.5° to 45°, and the C-SAPR VCP is 17 elevation angles ranging from 0.75° to 42°. Elevation angles for the setting ii) are equally distributed from 0.5° to 59.5° with a 1° increment; in total there are 60 elevation angles. This elevation setting intends to simulate rapid scanning radar observations.

The selection of the VCP (XR or LR) affects the density (spacing) and availability of observations at each height for gridding. Figures 2a and 2b show the coverage from the three radars for the retrieval domain for 3XR and 3LR VCPs, respectively. The cone of silence (absence of radar observations) from each radar is represented as yellow circle, in the middle of which the X-SAPR is located. Within the cone of silence of each radar, we only have two available radar measurements for the wind retrieval. In addition to the availability of radar observations, the spacing of the radar observations affect the quality of the gridding. Regions including few radar data points, particularly higher elevation angle regions for the XR VCP, may need to interpolate radar data at longer distances from the grid points. Figures 2c-2f show distance of the nearest radar data point at each grid box at heights of 1 km and 8 km for X-SAPR I6, and

Figs. 2g and 2h show normalized histograms of the nearest distance. At lower altitudes, the nearest distances in the entire retrieval domain (thin lines in Fig. 2h) are mostly less than 0.3 km for both VCPs. At higher altitudes (thin lines Fig. 2h), the distances of the nearest radar data points from the LR VCP are same as at lower altitudes, indicating that the LR VCP has similar radar data density at higher and lower altitudes. For the XR VCP, in contrast, many of grid boxes at 8 km AGL needed to use radar data at distances farther than 0.4 km, resulting in stronger smoothing when the gridding process.

2.4.3   Time duration of the radar VCP

Three time periods are considered here for the completion of the radar network VCP: i) snapshot (named Snap), where it is effectively assumed that the first WRF model output (at time 0 sec, top row, Fig. 3) is frozen in time and the radars instantaneously collect data according as their VCP without any cloud evolution; ii) a 2 minute (named 2min) radar network VCP to emulate the performance of rapid scanning radar networks; and iii) a 5 minute (named 5min) radar network VCP to emulate the performance of the ARM SGP network during MC3E and the performance of other mechanically-scanning radar networks. The 3FullGrid simulation (Sect. 2.4.1) uses a Snap VCP. The Snap VCP eliminates any concerns regarding advection and temporal evolution of the convective cloud and is used as benchmark of performance.

A set of WRF simulations at different times is used to construct the Plan Position Indicator (PPI) scans of the VCP; if a PPI scan takes more than 20 seconds, the WRF output in the following time step is used for the next PPI scan. An example demonstrating how different WRF model outputs are used in this experiment is shown in Fig. 3. Figure 3 shows horizontal cross sections of the Z and vertical velocity at 7 km and a vertical cross section of the at the area indicated with the solid line in the horizontal cross sections. The snapshot simulations use the WRF model output data at 12:18:00 UTC (top row). The 2-min VCP simulations use the WRF model output data from six consecutive model outputs extracted from 12:18:00 UTC to 12:19:40 UTC every 20 seconds. Each model output is used to forward simulate 3-4 PPI scans from the C-SAPR and the X-SAPRs when nominal (MC3E) VCP elevation angles are used (3XR and 4SR) and 10 PPI scans for X-SAPR simulations when the denser elevations angles VCP is simulated (3LR). The corresponding plots for the latest model output (12:19:40 UTC) used to forward

simulate the highest elevations of the 2-min VCP are shown in Fig. 3 (middle row). In accordance, the 5-min VCP simulations use the WRF data for 5 minutes composed of 15 snapshots ranging from 12:18:00 UTC to 12:22:40 UTC every 20 seconds. Each snapshot data was used for 1-2 PPI scans for C-SAPR and X-SAPR simulations with general VCP elevation angles (3XR and 4SR) and 4 PPI scans for denser VCP elevation angles (3LR). The corresponding plots for the 13th model output (4 minutes after the first scan, 12:22:00 UTC) used to forward simulate the highest elevations of the 5-min VCP simulations is shown in Fig. 3 (bottom row).

2.4.4 Advection correction

The high temporal resolution WRF output allows us to evaluate the impact of advection and evolution of the cloud field during the time period needed to complete the radar network VCP. If the cloud field was frozen (no cloud evolution), horizontal advection and wind shear are expected to tilt the cloud and dynamical structures in vertical. Advection schemes have been proposed to address this issue (e.g. Protat and Zawadzki, 1999; Shapiro et al., 2010b; Qiu et al., 2013). The present study used a reflectivity-based spatially-variable advection correction scheme described in Shapiro et al. (2010a) which allows trajectory of individual clouds and smooth grid-box-by-grid-box corrections of cloud locations. The advection correction procedure seeks to minimize a cost function that contains the frozen turbulence constraint and terms that confer spatial smoothness on the pattern-translation components and takes into account changes in cloud shape with time by using two different time PPI scans. The advection correction process is similarly implemented in this case.

The advection correction is applied between two similar elevation angle PPIs from consecutive VCPs. Each simulated Z field in PPI is converted and projected onto the two-dimensional (2D) Cartesian coordinate plane at a spatial resolution of 250 m. A weighting coefficient of the spatial smoothness terms in the cost function coefficient depends on the analysis grid spacing and the structure of the field being advected. An appropriate value of the coefficient can be determined by running some sensitivity tests. Based on preliminary tests (not shown), we deemed a coefficient of 300 dBZ^2 to be acceptable. Using two 2D Cartesian coordinated PPI data at two different times at the same elevation angle, the advection correction algorithm performs horizontal trajectory analysis of reflectivity and estimates the reflectivity

pattern translation components U and V on the 2D surfaces for each VCP elevation angle. The pattern translation components U and V fields, along with the associated trajectories of virtual particles moving with the reflectivity field, are then used to effect the advection correction of the radial wind field according to a time difference between a PPI scan and the base PPI scan, when creating the 3D Cartesian coordinated data. Such processed simulated radar measurements in 3D Cartesian coordinates are then incorporated into to the 3DVAR algorithm for the 3D wind retrieval as described in Sect. 2.3.

However, the cloud and dynamical field evolve while advected. This results in observing different cloud life stages by different PPI scans. Figure 3 (right column) shows a vertical cross-section of the vertical air motion within a convective cell that is tracked using the WRF model output. The location of the convective cell and vertical distributions of updrafts and downdrafts significantly vary from 12:18:00 UTC to 12:22:00 UTC. Thus, we need to consider that gridded radar observations collected after the completion of the VCP do not represent an actual snapshot of the 3D convective dynamics. Consequently, the mass continuity constraint will be applied in the column of gridded radar observations that is a mosaic of different stages of the lifetime of a convective element, and this, in turn, will limit the ability for this 3DVAR approach to satisfy the mass continuity equation (e.g., Clark et al., 1980; Gal-Chen, 1982), resulting in large potential uncertainties of the wind retrievals. The experiments presented here are designed to quantify the impact of cloud evolution on the retrieved wind field (Sect. 3.4).

3 Results

The evaluation of multi-Doppler radar-based velocity retrievals using independent observations is challenging to perform (e.g., Collis et al., 2013; North et al., 2017). Profiles of percentiles of updraft magnitudes are often used to evaluate numerical model results against vertical velocity retrievals from scanning Doppler radar networks and/or profiling radars (e.g., Wu et al., 2009; Varble et al., 2014; Fan et al., 2018). Here, we are interested in the estimation of the convective mass flux, thus, profiles of updraft morphology (number and area) and intensity (magnitude) are used to represent the impact of the selected sampling strategy.

3.1   Evaluation of multi-Doppler radar updraft property retrievals

Horizontal cross sections at 7 km AGL and vertical cross sections along y = 0 km of the retrieved vertical velocity field from the X-SAPR network, using the original grid (3FullGrid) and using the standard (XR) VCP for three different time periods (Snap, 2min and 5min) are shown in Fig. 4 (b, c, d, and e, respectively). The WRF model out at t = 0 (12:18:00 UTC) is also shown in Fig. 4a. The selection of the height of 7 km is based on the WRF model output analysis: the chosen height is the one with maximum updraft values. The WRF model output vertical velocity field indicates the presence of several cell-like, horizontally coherent updraft structures with updraft magnitude exceeding 5 m s^{-1}. The 3FullGrid simulation (Fig. 4b) provides results in good agreement with the original WRF vertical velocity field (Fig. 4a), suggesting that the 3DVAR wind retrieval algorithm is performed well.

The snapshot simulation (3XRSnap, Fig. 4c) provides results that are comparable to the original WRF vertical velocity field (Fig. 4a) and 3FullGrid retrieved vertical velocity field (Fig. 4b) at 7 km AGL, but slightly overestimates the updraft velocity above 8 km AGL. The 3XRSnap simulation reproduces the location and size of the stronger updraft areas defined with updraft magnitudes above 5 m s^{-1}, which show the cell-like structures, but it tends to have higher uncertainty in the areas around the location of strong convection (vertical velocity < 5 m s^{-1}). Updraft fractions for 1-5 m/s from the 3XRSnap simulation was overestimated by 0.1 – 0.17, which accounts for 40-88% of those from the WRF output. The uncertainty is attributed to the selected radar VCP due to gridding of sparse observations, rather than the 3DVAR wind retrieval algorithm. As increasing VCP time periods (2 min and 5 min) shown in Figs. 4d and 4e, respectively, the retrieved velocity features became less sharp, broader and shifted in space. The retrieved vertical velocity field shows the impact of interpolating the sparse observations (ring structures representing the poor X-SAPR sampling at 7 km) and the vertical velocity features appear elongated and connected.

At any vertical level in the WRF model output and in the retrieved 3D velocity field, a convective updraft core is defined as an area larger than 0.5 km^2 and with updraft velocities higher than 5 m s^{-1}. Figure 5a displays the profiles of the number of updraft cores from the 3FullGrid control wind retrieval simulation and from the WRF snapshot data at 12:18:00 UTC, WRF 2-min average (12:18:00-12:19:40), and WRF 5-min average (12:18:00-12:22:40). As expected, the 3FullGrid retrieved profile of number of

updraft cores captures very well the profile of the number of updraft cores in the WRF snapshot model output. Differences appear small between WRF Snap and 3FullGrid and are attributed to the potential uncertainty in the retrieval algorithm. The 2- and 5-min WRF output averaged profiles suggest that the number of convective updraft cores does not change over a period of 2 to 5 min. Figures 5b-e demonstrate

5   performance of the 3DVAR wind retrieval for several different configurations as described in Table 2. A noticeable departure between the WRF direct model output (number of updraft cores) and the estimated number of updraft cores above 6 km AGL is observed for all the detecting configurations with the exemption of the LR VCP. The use of a fourth radar or the implementation of the advection correction has little to no impact on the findings. The retrieved profiles of the number of coherent updrafts structures

10   show little sensitivity to the VCP time. This can be attributed to the fact that the number of updraft coherent structures does not change within 5 min required to complete all sampling strategies. Another possibility is that any stretching/distortion of the coherent structures due to cloud evolution and advection does not results to changes in the number of coherent structures.

     In a similar manner, the retrieved updraft fraction (UF), the retrieved convective mass flux (MF) and

15   the mean updraft velocity ($\overline{w}$) for the different VCPs are investigated and compared to the direct model output. In this study, convective mass flux (MF) is estimated at each height as:

$$MF = UF \; \overline{w} \; \overline{\rho_d} \; \; [kg \; s^{-1} \; m^{-2}] \tag{3}$$

where UF is updraft fraction over the domain, $\overline{w}$ is mean vertical velocity over the updraft area, and $\overline{\rho_d}$ is dry air density averaged over the domain. The updraft fraction and mean updraft velocity strongly

20   impact the domain averaged convective mass flux, which can be used to understand mass, energy and aerosol transport by the convective system.

     The analysis in this study is presented in Figs. 6, 7, and 8 for the two different updraft thresholds: 5 m s^{-1} (UF$_5$, MF$_5$, $\overline{w}_5$) and 10 m s^{-1} (UF$_{10}$, MF$_{10}$, $\overline{w}_{10}$). Furthermore, a comparison limited to a smaller domain where the higher density radar observations are available (squared area in Fig. 2) is added (Figs. 7g-i).

25   Each panel shows their profiles from the WRF snapshot at 12:18:00 by a black solid line (threshold of 5 m s^{-1}) and a black dashed line (threshold of 10 m s^{-1}) for the comparison. Table 3 presents root mean square errors (RMSEs) of UF, MF, and $\overline{w}$ profiles above 2 km AGL for all experiments.   In contrast to

the number of coherent updraft cores, the profiles of UF, MF and $\overline{w}$ exhibit larger sensitivity to the sampling parameters. In subsequent sections, a more detail analysis of the impact of the different options in the observational setup on the UF, MF and $\overline{w}$ profiles are discussed.

Figure 6 compares the WRF snapshot at 12:18:00, the WRF 2-min average, and the WRF 5-min average. The UF profiles from both WRF 2-min average and the WRF 5-min average are in very good agreement with that from WRF snapshot; this consistency is also shown in MF and $\overline{w}$ profiles (Figs. 6b and 6c, respectively), indicating that the updraft properties are statistically similar throughout the 5 minutes in this case. Figure 6 also compares the profiles from WRF outputs with those from the 3FullGrid simulation. As expected, the UF profiles from 3FullGrid simulation are in very good agreement with the WRF output for all thresholds (Fig. 6a, RMSE < 0.004), but show an underestimation by ~0.01 at 5.3 km AGL. For reference, 1% difference in the updraft fraction corresponds to 25 km^2 for a 50 km × 50 km retrieval domain. All the retrieved profiles of coherent updraft fraction exhibit considerable differences with the WRF output above 6 km AGL (Figs. 7 and 8). In general, the retrieved updraft fractions increase above 6 km AGL while the WRF output indicates that the updraft fraction decreases.

Figures 6b and 6c show MF and $\overline{w}$ profiles, respectively, from simulated wind retrievals for 3FullGrid together with those from the WRF output. The MF and $\overline{w}$ profiles in the Figures 6b and 6c are coupled with updraft areas for updraft values larger than 10 m s^{-1} (MF$_{10}$, $\overline{w}_{10}$) and for velocities lather than 5 m s^{-1} (MF$_5$, $\overline{w}_5$). For the WRF output, the peaks of MF values are found at heights between 5 and 7 km AGL, and the MF$_{10}$ values are generally the half of MF$_5$. The 3FullGrid simulation (Fig. 6b) well captures those features, but the maximum values at 5.25 km AGL are slightly underestimated as MF$_5$ decreases by up to 0.05 kg s^{-1} m^{-2} (RMSE of 0.02 kg s^{-1} m^{-2}). Since the $\overline{w}$ values are well estimated (RMSE of 0.15 m s^{-1} for $\overline{w}_5$), the underestimation is driven by the small underestimation of UF (by 0.01, Fig. 6a).

3.2 Effects of VCP elevation sampling and number of radars

The impact of the maximum elevation angle and density of elevation angles used in the VCP is easily demonstrated when comparing the 3XRSnap and 3LRSnap retrievals for the entire domain (Figs. 7a-f) or within the smaller domain (square area in Fig. 2, Figs. 7g-i). For all updraft parameters investigated here (number of updraft cores, UF, MF, and $\overline{w}$), the 3LRSnap produces improved comparisons to the direct

model output especially when limiting the evaluation area to the center square domain. The comparison for the number of cloud cores (Fig. 5) shows that 3XRSnap overestimated above 6.5 km. Figure 7a shows that UF_5 values from the 3XRSnap are overestimated above 6.5 km AGL, while UF_{10} values above 6.5 km are underestimated. These profiles indicate that updraft areas of 5-10 m s^{-1} are overestimated for the 3XRSnap retrievals, resulting in the overestimation of the number of updraft cores. This feature is also shown in other snapshots and 2-min VCP retrievals. The impact of a longer time VCP is more pronounced in the UF retrievals than the number of coherent updrafts cores. As in the case for the profile of the number of coherent updraft cores, the use of the LR VCP improves the updraft fraction profile retrievals. The errors generally increase with height above 6 km AGL. This result is similar to the dual-Doppler radar wind retrieval OSSE study for supercell storms by Potvin et al. (2012b).

The UF_{10} values from the 3XRSnap simulation are underestimated by 0.01 at 5-7 km AGL (~30 % of the true fraction, Fig. 7a) at higher altitudes above 5 km. The mean updraft velocities are also underestimated by 1 m s^{-1} for UF_{10} above 5.5 km (Fig. 7c). The underestimations in $\overline{w}_{10}$ and UF_{10} profiles result in underestimation of MF_{10}, and the maximum underestimation of 0.1 kg s^{-1} m^{-2} is found at 6 km AGL. For the threshold of 5 m s^{-1}, the overestimation of UF_5 above 7 km results in overestimation of MF_5, while the underestimation of the mean updraft velocity by 2 m s^{-1} above 4.5 km for UF_5 leads to the underestimation of MF_5 at 4.5-7 km AGL (Fig. 7b).

The mean updraft velocities for both UF_{10} ($\overline{w}_{10}$) and UF_5 ($\overline{w}_5$) from 3LRSnap slightly increase above 6 km AGL (Fig. 7d). Consequently, the MF_5 profile is improved as it increases at 4.5-7 km and decreases above 7 km (Fig. 7e, 24% decrease in RMSE). Similarly, the MF_{10} profile is also improved as it increases above 4.5 km, but it still underestimated by 0.05 kg s^{-1} m^{-2} at 5-9 km AGL (38% decrease in RMSE). Compared to the same VCP periods, the 3LR retrievals also show similar improvements at 2-min VCP and 5-min VCP. These results suggest that the VCP with dense elevation angles can improve the retrieval of strong updrafts with velocities larger than 10 m s^{-1}, and is more effective at higher altitudes (> 8 km).

Substantially improved retrievals can be obtained in a region near the CF where data density from each radar is higher (square region shown in Fig. 2). Figures 7g, 7h, and 7i show UF, MF, and $\overline{w}$, respectively, for the square region. The UF, $\overline{w}$, and hence MF are improved especially for 3LR simulations, where distances of nearest data are mostly less than 0.2 km (Figs. 2g and 2h). Although the profiles from

3XRSnap and 4SRSnap are improved as they capture the peak at middle altitude, the improvements are weaker than 3LR simulations at higher altitudes, where the distances of the nearest radar data points in the square region are similar as those from the entire domain for XR (Figs. 2g and 2h). It is suggested that the high data density should be considered as an indicator of improved retrievals, as long as the scanning the VCP is completed in 2 minutes.

Increasing the number of Doppler radars in retrievals would reduce the uncertainties as analyzed by Bousquet et al. (2008) and North et al. (2017). Here we compare the 4SRSnap simulation with the 3LRSnap and 3XRSnap simulations (Figs. 8a-c, Table 3). The 4SRSnap retrieval cannot significantly improve the UF_5 and UF_{10} profiles compared to those from the 3XRSnap, as well as the number of updraft cores and $\overline{w}$ profiles, and hence MF. Lower spatial resolutions of the C-SAPR VCP than the X-SAPR might induce more artifacts in the weaker updraft retrievals. The lower frequency radar (C-SAPR) can provide radar reflectivity measurements that may be easier to correct for hydrometeor and radome attenuation (e.g., Kurri and Huuskonen, 2008). In this case, it is perhaps advantageous to use the lower frequency radar to cover the domain sampled by the X-SAPR network. However, if additional radars of the same or better spatial resolution and VCP are available, the network architecture should be considered in order to maximize the triple-Doppler radar area by creating another sampling area with triple-Doppler radar observations.

3.3   Effect of VCP time period

The 2-min and 5-min time period VCP retrievals are compared to the snapshot retrievals to see how the VCP time periods affect the updraft retrievals. For the 3XR retrieval simulations, profiles of the number of updraft cores do not show significant differences among 3XRSnap, 3XR2min, and 3XR5min (Fig. 5b), consistent with little difference among those from WRFSnap, WRF2min, and WRF5min. This feature is also found in the 3LR simulations. However, some differences can be found in Figs. 7a-c, 7d-f, and 8a-c showing updraft fractions, convective mass flux, and mean updraft for 3XR, 3LR, and 3SR simulations. For both updraft threshold of 10 and 5 m s^{-1}, 3XR2min and 3XRSnap UF, $\overline{w}$, and hence MF are in close agreement at all altitudes and even with WRF output (WRFSnap and WRF2min) below 4.5 km, as well as with 3LR and 4SR simulations. The small impacts of 2-min time period are also found for

the center square region (Figs. 7g-i). For 3XR5min and 3LR5min simulations, however, UF_{10}, and $\overline{w}_{10}$ are significantly underestimated at 4-9 km AGL (50-110% increase in RMSE for UF_{10} and 40-55% increase in RMSE for $\overline{w}_{10}$ from snapshot simulations) when compared to the snapshot retrievals (3XRSnap and 3LRSnap, respectively). The differences from the 3XR5min simulation result in significant underestimation of MF_{10} at middle altitudes. These differences in UF and MF are also found even when comparing with the WRF UF/MF profiles averaged over 5 minutes (WRF5min). These features are common in 3XR, 3LR, and 4SR simulations.

The comparison of UF_5, $\overline{w}_5$, and MF_5 for different time period from a given VCP show different features compared to those for the larger updraft threshold. As discussed in Sect. 3.2, the UF_5 profiles from the simulations are largely overestimated above 6 km and cannot resolve a peak at middle altitudes. The difference becomes larger for the 5-min VCP retrieval simulations. It is suggested that a longer VCP time period tends to underestimate areas of larger updrafts (> 10 m s^{-1}) and overestimate areas of weaker updraft (< 10 m s^{-1}). On the other hand, $\overline{w}_5$ from 3XR5min is underestimated above 5 km. These errors in UF_5 and $\overline{w}_5$ from 3XR5min produce large underestimation of MF_5 at middle altitudes and overestimation above 7 km. These features are also shown in 3LR5min and 4SR5min, but the underestimations of MF_5 at middle altitudes are small, since underestimation of $\overline{w}_5$ is relatively small for 3LR5min or overestimation of UF_5 is larger for 4SR5min.

Overall, the impacts from the 2-min VCP on the updraft retrieval can be small, whereas the 5-min VCP can significantly intensify uncertainties especially for stronger updraft regions above 6 km AGL. This is likely due to small convective evolution in 2 minutes while large evolution and advection in 5 minutes as shown in Fig. 3. Potvin et al. (2012b) also showed a similar result that the data sampling in 3 minutes produced significant errors compared to shorter time period (1.5 min) and snapshot for supercell storms. Compared to the 3XR and 4SR retrievals for each VCP time period (2min and 5min), the 3LR2min and 3LR5min show better agreements.

3.4   Effect of Advection Correction

As presented in the previous section, the longer time VCPs more emphasize the uncertainties at upper levels. Because profiles of the updraft properties from WRF output do not change among the snapshot,

2-min average, and 5-min average, the differences found when comparing the simulated retrievals for 2-min and 5-min VCPs without advection correction and those for the snapshot VCPs are probably associated with i) imposed advection and ii) cloud evolution, rather than time change of the updraft properties. Advection will move clouds and cause mismatch of cloud locations between PPI scans from different radars and even from the same radar. Meantime, cloud evolution alters vertical and horizontal distributions of hydrometeors and vertical velocity, resulting in observing different cloud life stages by different PPI scans. Both issues result in deformation of cloud structures and may cause uncertainties in the wind retrieval algorithm, especially the mass continuity assumption is not satisfied adequately. The cloud locations can be corrected using an algorithm proposed by Shapiro et al. (2010a) as described in Sect. 2.4.4. Here, we compare 2-min and 5-min VCP experiments to which the advection correction has been applied (2minadv, 5minadv) with those without the advection correction and snapshot experiments to see how the advection correction can improve the retrievals using 2-min and 5-min VCPs.

Figures 8d-f show UF, MF, and $\overline{w}$ profiles, respectively, from the 2-min and 5-min VCP 3XR simulations corrected for advection (3XR2minadv and 3XR5minadv, respectively), together with those from WRF snapshot and 3XRSnap. The advection-corrected retrievals for the 2-min VCP well improve these profiles as they are closer to the WRF2min profiles and even to the snapshot retrieval (e.g., 16% decrease in RMSE of UF_5 from 3XR2min), while improvements are not significant for the 5-min VCP. Very similar improvements for the 2-min and 5-min VCPs by advection corrections are found in 3LR simulations with advection correction (not shown).

Figure 9 shows comparisons of vertical cross sections between wind retrievals obtained before and after applying the advection correction for the updraft core shown in Fig. 3 (right column). Chosen vertical cross sections go through the maximum updraft area at 7 km AGL. For the 2-min VCP retrievals, regions of updraft values > 5 m s^{-1} are significantly corrected by the advection correction technique and maintain the top-left to bottom-right tilt of the WRF updraft structure. It is clear (Fig. 3 right column) that within 5 min the updraft structure has evolved not only in its tilt but also by the presence of a downdraft near its lower levels. Thus, when using a 5-min VCP, a completely different updraft structure is reconstructed with different tilt and location of the maximum updraft velocity. The difficulty in improving the updraft retrieval using the advection correction, particularly for the 5-min VCP, is likely due to fast evolution of

convective clouds. The rapid evolution of the updraft structures simulated by the WRF are consistent with those from other modelling studies where the temporal evolution of the convective thermals can be significant over time periods larger than 2 min (e.g., Morrison et al., 2015; Hernández-Deckers and Sherwood, 2016).

4 Summary and conclusions

Convective motions affect microphysical processes and control the transport of moisture, momentum, heat, trace gases and aerosols from the boundary layer to the upper troposphere. Accurate characterization of the convective transport requires vertical air velocity retrievals especially in the middle and upper part of convective cloud systems, and multi-Doppler radar networks have been used to probe convection and provide wind retrievals including vertical air motion estimates. While there is a plethora of studies illustrating the ability of multi-Doppler radar observations to capture the low-level wind divergence and circulation, there is little to show regarding the capability of this observing system to capture the upper level convective dynamics. This study addressed potential observational sources of errors in triple-Doppler radar three-dimensional variational (3DVAR) updraft retrieval using a sophisticated forward radar simulator (CR-SIM) with the WRF simulation output for an MCS on 20 May 2011 during the Midlatitude Continental Convective Clouds Experiment (MC3E) for a domain of 50 km $\times$ 50 km $\times$ 10 km. An extensive sensitivity analysis is conducted to investigate impacts of radar volume coverage pattern (VCP), the number of radars used for the multi-Doppler radar analysis, time periods for VCP (2 and 5 minutes), and advection correction. An advection correction technique proposed by Shapiro et al. (2010a) was applied to the 2-min and 5-min VCP radar data. Updraft properties such as updraft fraction, mass flux, and updraft magnitude profiles with two different thresholds (5 m s^{-1} and 10 m s^{-1}), from simulated multi-Doppler radar wind retrievals using three X-band Scanning ARM Precipitation Radars (X-SAPRs) are examined. The number of updraft cores are also investigated with a threshold of 5 m s^{-1} at each height. The analysis results presented the following findings:

- As the previous literature has pointed out, the updraft fraction profiles from the simulated wind retrievals suggested that the selected VCP elevation strategy and radar sampling volume resolution affect uncertainties in upper-level (>4.5 km) updraft retrievals, owing to low density and low

resolution of radar data attributed to gaps between Plan Position Indicator (PPI) elevation angles and the radar sample volume increasing with distance from the radar. Those uncertainties increase with height above 6 km AGL. In overall experiments using VCPs, stronger updrafts > 10 m s^{-1} tend to be underestimated above 4.5 km, while areas of updrafts 5-10 m s^{-1} are overestimated above 6.5 km. Those impact the retrieval of convective mass flux.

- Increasing the maximum elevation angle and the density of the elevation angles of the radar VCP (i.e., 60° over elevation with 1° increment) can effectively improve the updraft retrieval, whereas an addition of data from a Doppler radar cannot significantly improve the updraft retrievals if the added radar VCP has inferior spatial resolutions.

- Shorter duration (2-min or less) radar VCPs are critical to producing high-quality vertical air motion retrievals. The 2-min VCP has small impacts on the snapshot updraft retrievals, but the 5-min VCP induces an important overestimation of areas of updrafts 5–10 m s^{-1} above 6.5 km, underestimation of updrafts > 10 m s^{-1} at 4.5 – 8 km, and overestimation of updrafts > 10 m s^{-1} above 8-9 km.

- The advection correction works to improve the updraft fraction and mean updraft profiles as the profiles become closer to those from the snapshot retrievals and time averaged updraft fields, but it is still challenging to improve stronger updraft retrievals especially for 5-min VCP due to the rapid deformation of the dynamical structures in the simulated mesoscale convective system. The magnitude of improvement by the increase of elevation angles is larger than that by advection correction, even though the VCP needs 2 minutes. However, for the increasing elevations taking 5 minutes, the improvement is less than that from the original VCP completed within 2 minutes.

Gridding technique is also an important factor to determine the uncertainties in the wind retrievals. Sophisticated gridding techniques to cover the three-dimensional analysis domain at high spatial resolution, even for higher altitudes, tend to suppress the uncertainty (e.g., Majcen et al., 2008; Collis et al., 2010; North et al., 2017). Another error source that we did not consider in this study is hydrometeor fall speed estimate, which is generally estimated from radar reflectivity. The sophisticated attenuation correction techniques especially for shorter wavelength radars (e.g., Kim et al, 2008; Gu et al., 2011) and

best estimates of hydrometeor fall speeds (Giangrande et al., 2013) are required to reduce the wind retrieval uncertainties.

In brief, the retrieval of the high-quality vertical velocities in the upper part of convective clouds is very challenging, while the multi-Doppler radar vertical velocity retrievals have been conventionally used to evaluate the CRM simulated dynamical fields. Some of the CRM simulations significantly overestimated compared to multi-Doppler radar vertical velocity retrievals (e.g., Varble et al., 2014; Fan et al., 2017). The present study would suggest that the multi-Doppler radar retrievals for MCSs tend to underestimate the updraft values at middle and upper levels and need to be carefully used considering the limitations of the radar observing system. The assessment of the multi-Doppler radar retrieval presented in this study could vary for different storm characteristics (e.g., isolated storm and less wind shear).

Although the present study focused on the ARM X-band radar network, the similar dense radar network has been installed in several regions (e.g., Bousquet et al., 2007; Maesaka, et al. 2011; Helmert et al., 2014), and field campaigns targeting deep convection (past, on-going and future) would be strongly motivated to install multiple Doppler radars to observe vertical air motions in convective clouds. The present analysis can give valuable information to improve the observation strategies and decide optimized scan strategies for the networks. Most of the improvements required in the sampling strategy of the observing system (higher maximum elevation angle, higher density elevation angles and rapid VCP time period) can be accomplished using rapid scan radar systems such as the Doppler on Wheels mobile radars (DOWs) or even phased array radar systems. However, even when such rapid scan radar networks are available, the multi-Doppler retrieval spatial domain will be fairly small compared to the entire radar network coverage. Despite of the limited domain, the observations do cover enough area to track isolated convective updrafts and contain enough samples to derive reliable, low-uncertainty estimates of updraft and downdrafts properties in convective clouds. Spaceborne radar systems with Doppler velocity capability such as the Earth Clouds Aerosols and Radiation Explorer (EarthCARE, Illingworth et al., 2015; Kollias et al., 2018b) or future spaceborne radar concepts (Tanelli et al., 2018) are expected to provide additional middle and upper level convective velocity observations especially over the tropical oceans.

Acknowledgements

Portions of this work are funded by the U.S. DOE Office of Science's Biological and Environmental Research Program through the Atmospheric Radiation Measurement (ARM) and Atmospheric System Research (ASR) programs. P. Kollias is also supported by U.S. DOE grant DE‑ SC0012704. The contribution of A. Shapiro has been supported by NSF grant AGS-1623626. The source code and user manual for the Cloud Resolving Model Radar Simulator (CR-SIM) are available at https://www.bnl.gov/CMAS/cr-sim.php.

References

Barnes, S. L.: A technique for maximizing details in numerical weather map analysis, J. Appl. Meteor., 3, 396–409, doi: 10.1175/1520-0450(1964)003<0396:ATFMDI>2.0.CO;2, 1964.

Bell, M. M., Montgomery, M. T., and Emanuel, K. A.: Air–sea enthalpy and momentum exchange at major hurricane wind speeds observed during CBLAST. J. Atmos. Sci., 69, 3197–3222, doi: 10.1175/JAS-D-11-0276, 2012.

Bousquet, O. and Chong, M.: A Multiple-Doppler Synthesis and Continuity Adjustment Technique (MUSCAT) to recover wind components from Doppler radar measurements, J. Atmos. Oceanic Technol., 15, 343–359, doi: 10.1175/1520-0426(1998)015<0343%3AAMDSAC>2.0.CO%3B2, 1998.

Bousquet, O., Tabary, P., and Parent du Châtelet, J.: On the value of operationally synthesized multiple-Doppler wind fields, Geophys. Res. Lett., 34, L22813, doi:10.1029/2007GL030464, 2007.

Bousquet, O., Tabary, P., and Parent du Châtelet, J.: Operational multiple-Doppler wind retrieval inferred from long-range radial velocity measurements, J. Appl. Meteor. Climatol., 47, 2929-2945, doi: 10.1175/2008JAMC1878.1, 2008.

Byers, H. R. and Braham, R. R.,: Thunderstorm structure and circulation, J. Meteor., 5, 71–86, 1948, doi: 10.1175/1520-0469(1948)005<0071:TSAC>2.0.CO;2, 1948.

Caya, A.: Assimilation of radar observations into a cloud-resolving model, Ph.d., McGill University, Montreal, Quebec, 2001.

Chong, M. and Campos, C.: Extended overdetermined dual-Doppler formalism in synthesizing airborne Doppler radar data, J. Atmos. Oceanic Technol. 13, 581-597, doi: 10.1175/1520-0426(1996)013<0581:EODDFI>2.0.CO;2, 1996.

Chong, M. and Testud, J.: Three-dimensional air circulation in a squall line from airborne dual-beam Doppler radar data: A test of coplane methodology software, J. Atmos. Oceanic Technol. 13, 36-53, doi: 10.1175/1520-0426(1996)013<0036%3ATDACIA>2.0.CO%3B2, 1996.

Clark, T. L., Harris, F. I., and Mohr, C. G.: Errors in wind fields derived from multiple-Doppler radars: Random errors and temporal errors associated with advection and evolution, J. Appl. Meteor., 19, 1273–1284, 1980.

Collis, C., Protat, A., May, P. T., and Williams, C.: Statistics of storm updraft velocities from TWP-ICE including verification with profiling measurements, J. Appl. Meteor. Climatol., 52, 1909-1922, doi: 10.1175/JAMC-D-12-0230.1, 2013.

Collis, S., Protat, A., and Chung, K.-S.: The effect of radial velocity gridding artifacts on variationally retrieved vertical velocities. J. Atmos. Oceanic Technol., 27, 1239–1246, 2010.

Cressman, G. P.: An operational objective analysis system, Mon. Wea. Rev., 87, 367–374, doi: 10.1175/1520-0493(1959)087<0367:AOOAS>2.0.CO;2, 1959.

Dolan, B. A., and Rutledge, S. A.: An integrated display and analysis methodology for multivariable radar data. J. Appl. Meteor. Climatol., 46, 1196–1213, doi: 10.1175/JAM2524.1, 2007.

Donner, L. J., Seman, C. J., Hemler, R. S., and Fan, S.: A cumulus parameterization including mass fluxes, convective vertical velocities, and mesoscale effects: Thermodynamic and hydrological aspects in a general circulation model, J. Climate, 14, 3444–3463, doi: 10.1175/1520-0442(2001)014<3444:ACPIMF>2.0.CO;2, 2001.

Donner, L. J., O'Brien, T. A., Rieger, D., Vogel, B., and Cooke, W. F.: Are atmospheric updrafts a key to unlocking climate forcing and sensitivity?, Atmos. Chem. Phys., 16, 12983-12992, doi:10.5194/acp-16-12983-2016, 2016.

Fan, J., Han, B., Varble, A., Morrison, H., North, K., Kollias, P., Chen, B., Dong, X., Giangrande, S. E., Khain, A., Lin, Y., Mansell, E., Milbrandt, J. A., Stenz, R., Thompson, G., and Wang, Y.: Cloud-

resolving model intercomparison of an MC3E squall line case: Part I—Convective updrafts, J. Geophys. Res. Atmos., 122, 9351–9378, doi:10.1002/2017JD026622, 2017.

Fridlind, A. M., Li, X., Wu, D., van Lier-Walqui, M., Ackerman, A. S., Tao, W.-K., McFarquhar, G. M., Wu, W., Dong, X., Wang, J., Ryzhkov, A., Zhang, P., Poellot, M. R., Neumann, A., and Tomlinson J. M.: Derivation of aerosol profiles for MC3E convection studies and use in simulations of the 20 May squall line case, Atmos. Chem. Phys., 17, 5947-5972, doi: 10.5194/acp-17-5947-2017, 2017.

Friedrich, K. and Hagen, M.: Wind synthesis and quality control of multiple-Doppler-derived horizontal wind fields, J. Appl. Meteor., 43, 38-57, doi:10.1175/1520-0450(2004)043<0038:WSAQCO>2.0.CO;2, 2004.

Gal-Chen, T.: Errors in fixed and moving frame of references: Applications for conventional and Doppler radar analysis, J. Atmos. Sci., 39, 2279–2300, 1982.

Gao, J., Xue, M., Shapiro, A., and Droegemeier, K. K.: A variational method for the analysis of three-dimensional wind fields from two Doppler radars, Mon. Wea. Rev., 127, 2128–2142, doi: 10.1175/1520-0493(1999)127<2128:AVMFTA>2.0.CO;2, 1999.

Giangrande, S. E., Collis, S., Straka, J., Protat, A., Williams, C., and Krueger, S.: A summary of convective-core vertical velocity properties using ARM UHF wind profilers in Oklahoma, J. Appl. Meteor. Climatol, 52, 2278-2295, doi: 0.1175/JAMC-D-12-0185.1, 2013.

Given, T. and Ray, P. S.: Response of a two-dimensional dual-Doppler radar wind synthesis, J. Atmos. Ocean. Tech., 11, 239-255, doi: 10.1175/1520-0426(1994)011<0239:ROATDD>2.0.CO;2, 1994.

Gu, J.-Y., Ryzhkov, A., Zhang, P., Neilley, P., Knight, M., Wolf, B., and Lee, D.-I.: Polarimetric attenuation correction in heavy rain at C band. J. Appl. Meteor. Climatol, 50, 39-58, doi: 10.1175/2010JAMC2258.1, 2011.

Hartmann, D.L., Hendon, H.H., and Houze Jr., R.A.: Some implications of the mesoscale circulations in cloud clusters for large-scale dynamics and climate, Journal of the Atmospheric Sciences, 41, 113-121, doi: 10.1175/1520-0469(1984)041<0113:SIOTMC>2.0.CO;2, 1984.

Helmert, K., and Coauthors: DWDs new radar network and post-processing algorithm chain. *Proc. Eighth European Conf. on Radar in Meteorology and Hydrology (ERAD 2014)*, Garmisch-Partenkirchen,

Germany, DWD and DLR, 4.4, 2014. [Available online at http://www.pa.op.dlr.de/erad2014/programme/ExtendedAbstracts/237_Helmert.pdf]

Helmus, J. and Collis, S.: The Python ARM Radar Toolkit (Py-ART), a library for working with weather radar data in the Python programming language, Journal of Open Research Software, 4, p.e25, 2016.

5   Heymsfield, G. M., Tian, L., Heymsfield, A. J., Li, L., and Guimond, S.: Characteristics of deep tropical and subtropical convection from nadir-viewing high-altitude airborne Doppler radar, J. Atmos. Sci., 67, 285–308, doi: https://doi.org/10.1175/2009JAS3132.1, 2010.

Illingworth, A. I., and Coauthors.: The EarthCARE satellite: The next step forward in global measurements of clouds, aerosols, precipitation, and radiation, Bull. Amer. Meteor. Soc., 96 (8),
10   1311-1332, doi: 10.1175/BAMS-D-12-00227.1, 2015.

Jensen, M. P. and Coauthors: The Midlatitude Continental Convective Clouds Experiment (MC3E), Bull. Amer. Meteor. Soc., 1667-1686, doi: 10.1175/BAMS-D-14-00228.1, 2016.

Jorgensen, D. P. and LeMone, M. A.: Vertically velocity characteristics of oceanic convection, J. Atmos. Sci., 46, 621–640, doi: 10.1175/1520-0469(1989)046<0621:VVCOOC>2.0.CO;2, 1989.

15 Junyent, F., Chandrasekar, V., McLaughlin, D., Insanic, E., and Bharadwaj, N.: The CASA Integrated Project 1 Networked Radar System. *J. Atmos. Oceanic Technol.,* **27**, 61–78, doi: 10.1175/2009JTECHA1296.1, 2010.

Isom, B., and Coauthors: The atmospheric imaging radar: Simultaneous volumetric observations using a phased array weather radar. *J. Atmos. Oceanic Technol.*, **30**, 655–675, doi: 10.1175/JTECH-D-12-
20   00063.1, 2013.

Kim, D.-S., Maki, M., Lee, D.-I.: Correction of X-band radar reflectivity and differential reflectivity for rain attenuation using differential phase, Atmospheric Research, 90, 1-9, doi: 10.1016/j.atmosres.2008.03.001, 2008.

Kingsmill, D. E. and Houze, Jr., R. A.: Kinematic characteristics of air flowing into and out of
25   precipitating convection over the west Pacific warm pool: An airborne Doppler radar survey, *Q. J. Roy. Meteorol. Soc*., 125, 1165–1270, doi: https://doi.org/10.1002/qj.1999.49712555605, 1999.

Kumar, V. V., Jakob, C., Protat, A., Williams, C. R., and May, P. T.: Mass-flux characteristics of tropical cumulus clouds from wind profiler observations at Darwin, Australia, J. Atmos. Sci., 72, 1837–1855, doi: 10.1175/JAS-D-14-0259.1, 2015.

Kollias, P., McLaughlin, D. J., Frasier, S., Oue, M., Luke, E., and Sneddon, A.: Advances and applications in low-power phased array X-band weather radars. Proc. 2018 IEEE Radar Conference, Oklahoma City, OK, USA, doi: 10.1109/RADAR.2018.8378762, 2018a.

Kollias, P., A. Battaglia, A. Tatarevic, K. Lamer, F. Tridon and L. Pfitzenmaier: The EarthCARE cloud profiling radar (CPR) Doppler measurements in deep convection: challenges, post-processing and science applications. Proc. SPIE 10776, Remote Sensing of the Atmosphere, Clouds and Precipitation doi:10.1117/12.2324321, 2018b.

Kurri, N. and Huuskonen, A.: Measurements of the transmission loss of a radome at different rain intensities, *J. Atmos. Oceanic Technol.*, **25**, 1590–1599, doi: 10.1175/2008JTECHA1056.1, 2008.

LeMone, M. A. and Zipser, E. J.: Cumulonimbus vertical velocity events in GATE. Part I: Diameter, intensity and mass flux, J. Atmos. Sci., 37, 2444–2457, doi: 10.1175/1520-0469(1980)037<2444:CVVEIG>2.0.CO;2 1980.

Lenschow, D. H.: Estimating updraft velocity from an airplane response, Mon. Wea. Rev., 104, 618–627, doi: 10.1175/1520-0493(1976)104<0618:EUVFAA>2.0.CO;2, 1976.

Lhermitte, R. and Miller, L.: Doppler Radar Methodology for the Observation of Convective Storms. 14th Conf. on Radar Meteor., Tuscon, AZ, *Amer. Meteor. Soc.,* 133-138, 1970.

Liu, Y.-C., Fan, J., Zhang, G. J., Xu, K.-M., and Ghan, S. J.: Improving representation of convective transport for scale-aware parameterization: 2. Analysis of cloud-resolving model simulations, J. Geophys. Res. Atmos.,120, 3510–3532, doi:10.1002/2014JD022145, 2015.

Maesaka, T., Maki, M., Iwanami, K., Tsuchiya, S., Kieda, K., and Hoshi, A.: Operational rainfall estimation by X-band MP radar network in MLIT, Japan. Proc. 35th Int. Conf. on Radar Meteorology, Pittsburgh, PA, Amer. Meteor. Soc., 142. 2011. [Available online at https://ams.confex.com/ams/35Radar/webprogram/Paper191685.html.]

Majcen, M., P. Markowski, Y. Richardson, D. Dowell, J. Wurman: Multipass objective analyses of Doppler radar data., J. Atmos. Ocean. Tech., 25, 1845 − 1858, doi: 10.1175/2008JTECHA1089.1, 2008.

Mather, J. H., and Voyles, J. W.: The Arm Climate Research Facility: A review of structure and capabilities, Bull. Amer. Meteor. Soc., 94, 377–392, doi: 10.1175/BAMS-D-11-00218.1, 2013.

Miller, L. J., and Fredrick, S. M.: Custom Editing and Display of Reduced Information in Cartesian space (CEDRIC) manual. National Center for Atmospheric Research, Mesoscale and Microscale Meteorology Division, Boulder, CO, 130 pp, 1998.

Morrison, H., Morales, A., and Villanueva-Birriel, C.: Concurrent Sensitivities of an Idealized Deep Convective Storm to Parameterization of Microphysics, Horizontal Grid Resolution, and Environmental Static Stability. Monthly Weather Review, 143(6), 2082–2104. http://doi.org/10.1175/MWR-D-14-00271.1,2015.

Morrison, H., Curry, J., and Khvorostyanov, V.: A new double-moment micro-physics parameterization for application in cloud and climate models. Part I: Description, J. Atmos. Sci., 62, 1665–1677, doi:10.1175/JAS3446.1, 2005.

North, K. W., Oue., M., Kollias, P., Giangrande, S. E., Collis, S. M., and Potvin, C. K.: Vertical air motion retrievals in deep convective clouds using the ARM scanning radar network in Oklahoma during MC3E, Atmos. Meas. Tech. 10, 1 − 14, doi: 10.5194/amt-10-2785-2017, 2017.

Oue, M., Inagaki, K., Shinoda, T., Ohigashi, T., Kouketsu, T., Kato, M., Tsuboki, K., Uyeda H.: Polarimetric Doppler radar analysis of organization of a stationary rainband with changing orientations in July 2010, J. Meteorol. Soc. Jpn., 22, 457-481, doi: 10.2151/jmsj.2014-503, 2014.

Park, S-G. and Lee, D-K.: Retrieval of High-Resolution Wind Fields over the Southern Korean Peninsula Using the Doppler Weather Radar Network. *Wea. Forecasting,* **24**,87–103, https://doi.org/10.1175/2008WAF2007084.1, 2009.

Pazmany, A. L., Mead, J. B., Bluestein, H. B., Snyder, J. C., and Houser, J. B.: A mobile rapid-scanning X-band polarimetric (RaXPol) Doppler radar system. *J. Atmos. Oceanic Technol.*, **30**, 1398–1413, doi: 10.1175/JTECH-D-12-00166.1, 2013.

Potvin, C. K., Betten, D., Wicker, L. J., Elmore, K. L., and Biggerstaff, M. I.: 3DVAR versus traditional dual-Doppler wind retrievals of a simulated supercell thunderstorm, Mon. Wea. Rev., 140, 3487–3494, doi: 10.1175/MWR-D-12-00063.1, 2012a.

Potvin, C. K., Wicker, L. J., and Shapiro A.: Assessing errors in variational dual-Doppler wind syntheses of supercell thunderstorms observed by storm-scale mobile radars, J. Atmos. Ocean. Tech., 29, 1009–1025, doi: 10.1175/JTECH-D-11-00177.1, 2012b.

Protat, A., and Zawadzki, I.: A variational method for real-time retrieval of three-dimensional wind field from multiple-Doppler bistatic radar network data. *J. Atmos. Oceanic Technol*, **16,** 432–449, doi: 10.1175/1520-0426(1999)016<0432:AVMFRT>2.0.CO;2, 1999.

Qiu, X., Xu, Q., Qiu, C., Nai, K., and Zhang, P.: Retrieving 3D wind field from phased array radar rapid scans. Advances in Meteorology, 2013, 792631, 1-16, doi: 10.1155/2013/792631, 2013.

Shapiro, A., Willingham, K. M., and Potvin, C. K.: Spatially variable advection correction of radar data. Part I: Theoretical considerations, J. Atmos. Sci., 67, 3445-3456, doi: 10.1175/2010JAS3465.1, 2010a.

Shapiro, A., Willingham, K. M., and Potvin, C. K.: Spatially variable advection correction of radar data. Part II: Test Results, J. Atmos. Sci., 67, 3457-3470, doi: 10.1175/2010JAS3466.1, 2010b.

Sherwood, S. C., Bony, S., and Dufresne, J.-L.: Spread in model climate sensitivity traced to atmospheric convective mixing. Nature, 505, 37-42. Doi:10.1038/nature12829, 2014.

Steiner, M.: A new relationship between mean Doppler velocity and differential reflectivity, J. Atmos. Oceanic Technol., 8, 430–443, 1991.

Su, J., B. Xiang, B. Wang, ad T. Li: Abrupt termination of the 2012 Pacific warming and its implication on ENSO prediction. Geophys. Res. Lett., 41, 9058-9064. doi:10.1002/2014GL062380, 2014.

Stonitsch, J.R. and Markowski, P.M.: Unusually Long Duration, Multiple-Doppler Radar Observations of a Front in a Convective Boundary Layer. *Mon. Wea. Rev.,* **135,** 93–117, https://doi.org/10.1175/MWR3261.1, 2007.

Tanelli, S., Haddad, Z. S., Im, E., Durden, S. L., Sy, O. O., Peral, E., Sadowy, G. A., Sanchez-Barbetty, M.: Radar concepts for the next generation of spaceborne observations of cloud and precipitation

processes. IEEE Proceedings of Radar Conference, Oklahoma City, OK, doi: 10.1109/RADAR.2018.8378741, 2018.

Tao, W.-K., Wu, D., Lang, S., Chern, J.-D., Peters-Lidard, C., Fridlind, A., and Matsui, T.: High-resolution NU-WRF simulations of a deep convective-precipitation system during MC3E: Further improvements and comparisons between Goddard microphysics schemes and observations, J. Geophys. Res. Atmos., 121, 1278–1305, doi:10.1002/2015JD023986, 2016.

Tatarevic, A., Kollias, P., Oue, M., Wang, D., and Yu, K.: User's Guide CR-SIM SOFTWARE v 3.1, Brookhaven National Laboratory - Stony Brook University - McGill University Radar Science Group, 2018. [Available at https://www.bnl.gov/CMAS/cr-sim.php.]

Timmermans, R. M. A., Schaap, M., and Builtjes, P.: An Observing System Simulation Experiment (OSSE) for Aerosol Optical Depth from Satellites, J. Atmos. Ocean. Tech., 2673 – 2682, doi: 10.1175/2009JTECHA1263.1, 2009.

Varble, A., Zipser, E. J., Fridlind, A. M., Zhu, P., Ackerman, A. S., Chaboureau, J.-P., Collis, S., Fan, J., Hill, A., and Shipway, B.: Evaluation of cloud-resolving and limited area model intercomparison simulations using TWP-ICE observations: 1. Deep convective updraft properties, J. Geophys. Res. Atmos., 119, 13,891–13,918, doi:10.1002/2013JD021371, 2014.

Wakasugi, K., Mizutani, A., Matsuo, M., Fukao, S., and Kato, S. : A direct method for deriving drop-size distribution and vertical air velocities from VHF Doppler radar spectra. *J. Atmos. Oceanic Technol.*, **3**, 623–629, doi: 10.1175/1520-0426(1986)003<0623:ADMFDD>2.0.CO;2, 1986.

Williams, C. R.: Vertical Air Motion Retrieved from Dual-Frequency Profiler Observations. *J. Atmos. Oceanic Technol.,* **29**, 1471–1480, https://doi.org/10.1175/JTECH-D-11-00176.1, 2012.

Wu, J., Del Genio, A. D., Yao, M., and Wolf, A. B.: WRF and GISS SCM simulations of convective updraft properties during TWP-ICE, J. Geophys. Res., 114 (D4), D04206, doi: 10.1029/2008JD010851, 2009.

Wu, W. and McFarquhar, G. M.: On the impacts of different definitions of maximum dimension for nonspherical particles recorded by 2D imaging probes, J. Atmos. Ocean. Tech., 33, 1057-1072, doi: 10.1175/JTECH-D-15-0177.1, 2016.

Wurman, J., The DOW mobile multiple-Doppler network. Preprints, 30th Int. Conf. on Radar Meteorology, Munich, Germany, Amer. Meteor. Soc., 95–97, 2001.

Tables and figures

Table 1: Simulated radar configurations and measurement strategy.

	X-SAPR	C-SAPR
Radar frequency (GHz)	9.5	5.5
Beamwidth (degrees)	1.1	1.0
Number of elevation angles	21	17
Elevation angles (degrees)	0.5, 1.5, 2.5, 3.5, 4.5, 5.5, 6.5, 7.5, 8.5, 9.5, 10.5, 11.5, 12.5, 14.0, 17.0, 20.0, 25.0, 30.0, 35.0, 40.0, 45.0	0.8, 1.2, 1.9, 2.6, 3.5, 4.4, 5.3, 6.4, 7.8, 9.6, 11.7, 14.3, 17.5, 21.4, 26.1, 33.0, 42.0
Azimuth spacing (degrees)	1.1	1.0
Maximum observation range (km)	40	120
Range gate spacing (m)	60	120
Radar location	X-SAPRs (I4, I5, and I6) of Fig. 1	C-SAPR I7 of Fig.1
Antenna rotation rate* (° s^{-1})	28	18

5   * Antenna rotation rates used during the MC3E are presented and not used in this study.

Table 2: Overview and short description of the different sensitivity simulations.

Simulation	Name	Specification
Control	3FullGrid	i) All elevation angles from 3 X-SAPRs at each grid box of the original WRF snapshot grid at 12:18:00 UTC (no interpolation according to the radar beamwidth is considered
Radar VCP	3XR	i) 3 X-SAPRs with 21 elevation angles ranging from 0.5 to 45 degrees over elevation angle
	3LRs	ii) 3 X-SAPRs with 60 elevation angles ranging from 0.5 to 59.5 degrees with equal increment of 1 degree
	4SR	iii) 4 radars including 3 X-SAPRs and the C-SAPR
Time period	Snap	i) Snapshot at 12:18:00
	2min	ii) 2 minutes (6 snapshots)
	5min	iii) 5 minutes (15 snapshots)
Advection correction	(No name)	i) No advection correction
	adv	ii) Advection correction proposed by Shapiro et al. (2010a) for time settings ii) and iii)

Table 3: Root mean square error (RMSE) of UF_5, UF_{10}, MF_5, MF_{10}, $\bar{w}_5$, and $\bar{w}_{10}$ profiles above 2 km AGL for all experiments.

	UF_5	UF_{10}	MF_5 [kg m^{-2} s^{-1}]	MF_{10} [kg m^{-2} s^{-1}]	$\bar{w}_5$ [m s^{-1}]	$\bar{w}_{10}$ [m s^{-1}]
3FullGrid	0.34×10^{-2}	0.18×10^{-2}	0.23×10^{-1}	0.18×10^{-1}	0.15	1.93
3XRSnap	3.06×10^{-2}	0.68×10^{-2}	0.89×10^{-1}	0.60×10^{-1}	1.18	0.65
3XR2min	3.45×10^{-2}	0.63×10^{-2}	1.02×10^{-1}	0.52×10^{-1}	1.10	0.53
3XR5min	3.26×10^{-2}	1.03×10^{-2}	1.08×10^{-1}	0.95×10^{-1}	1.48	1.01
3LRSnap	1.99×10^{-2}	0.42×10^{-2}	0.68×10^{-1}	0.37×10^{-1}	0.87	0.50
3LR2min	2.44×10^{-2}	0.49×10^{-2}	0.85×10^{-1}	0.41×10^{-1}	0.91	0.52
3LR5min	3.94×10^{-2}	0.92×10^{-2}	1.37×10^{-1}	0.75×10^{-1}	1.23	0.70
4SRSnap	3.57×10^{-2}	0.64×10^{-2}	1.04×10^{-1}	0.56×10^{-1}	1.12	0.67
4SR2min	3.43×10^{-2}	0.66×10^{-2}	1.04×10^{-1}	0.57×10^{-1}	1.06	0.56
4SR5min	5.79×10^{-2}	1.10×10^{-2}	1.91×10^{-1}	0.83×10^{-1}	1.33	0.81
3XR2minadv	2.90×10^{-2}	0.75×10^{-2}	0.96×10^{-1}	0.65×10^{-1}	1.11	0.61
3XR5minadv	3.38×10^{-2}	0.96×10^{-2}	1.10×10^{-1}	0.88×10^{-1}	1.28	0.89
3LR2minadv	1.39×10^{-2}	0.71×10^{-2}	0.64×10^{-1}	0.64×10^{-1}	0.90	0.66
3LR5minadv	1.55×10^{-2}	1.15×10^{-2}	0.85×10^{-1}	1.02×10^{-1}	1.40	0.85
3XRSnap (limited area)	5.09×10^{-2}	1.29×10^{-2}	1.53×10^{-1}	1.08×10^{-1}	1.06	2.86
3XR2min (limited area)	4.73×10^{-2}	1.48×10^{-2}	1.69×10^{-1}	1.20×10^{-1}	0.86	0.96
3LRSnap (limited area)	2.24×10^{-2}	0.89×10^{-2}	0.79×10^{-1}	0.83×10^{-1}	0.71	2.87
3LR2min (limited area)	2.19×10^{-2}	1.28×10^{-2}	0.84×10^{-1}	1.19×10^{-1}	0.81	0.88
4SRSnap (limited area)	5.83×10^{-2}	1.11×10^{-2}	1.74×10^{-1}	0.94×10^{-1}	0.93	2.84
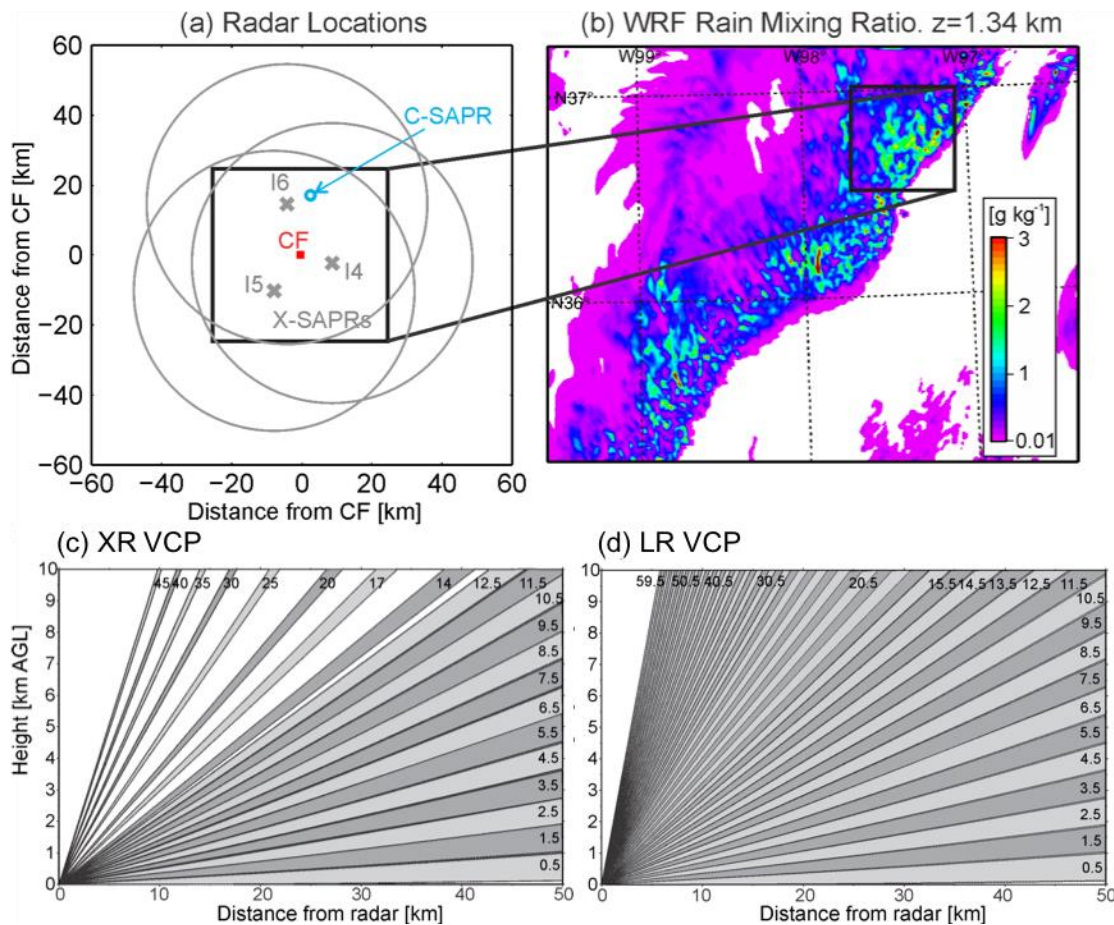
Figure 1: (a) Locations of the simulated X-band Scanning ARM Precipitation Radars (X-SAPRs) and the Department of Energy Atmospheric Radiation Measurements (ARM) Central Facility. Large gray circles represent maximum range of each X-SAPR. (b) Rain water mixing ratios at 1.3 km altitude from the WRF simulation of a mesoscale convective system at 12:18:00 UTC on 20 May 2011. Black boxes represent the domain used for wind retrievals. (c and d) Elevation coverage for X-SAPR general VCP (XR) and high-density elevation VCP (LR), respectively.
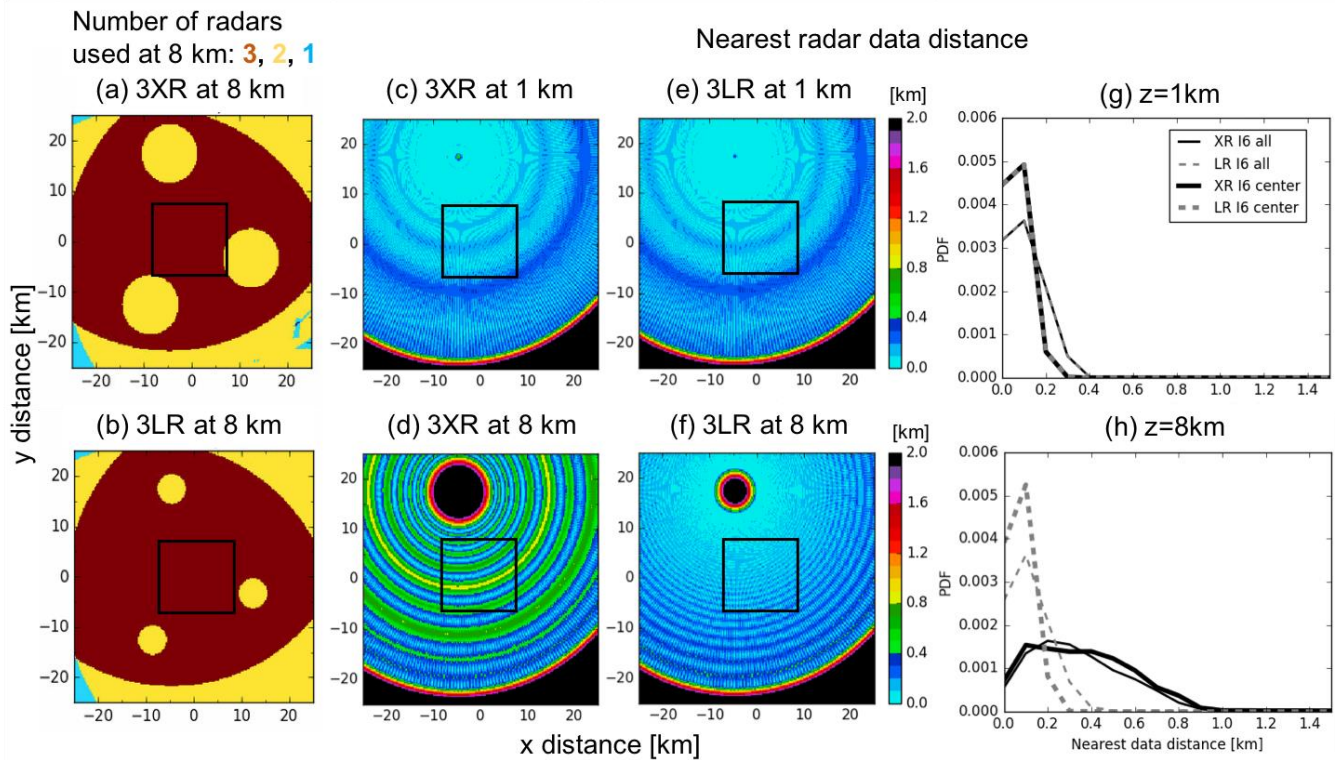
Figure 2: (a and b) The number of radars used for retrievals at each grid box at 8 km above ground level (AGL) for 3XR VCP (a) and 3LR VCP (b), (c-f) distance of nearest radar data point at each grid box at 1 km (c and e) and 8 km (d and f) AGL for the radar location of I6 with XR VCP (c and d) and LR VCP (e and f), and (g and h) histograms of the distance of nearest radar data point at 1 km (g) and 8 km (h) AGL normalized by the total number of data samples and the nearest distance bin size (0.1 km). In panels g and h, black sold lines represent the radar location of I6 with XR VCP, gray dashed lines represent the radar location of I6 with LR VCP, thin lines represent the entire horizontal domain, and thick lines represent a box area shown in panels a-f.
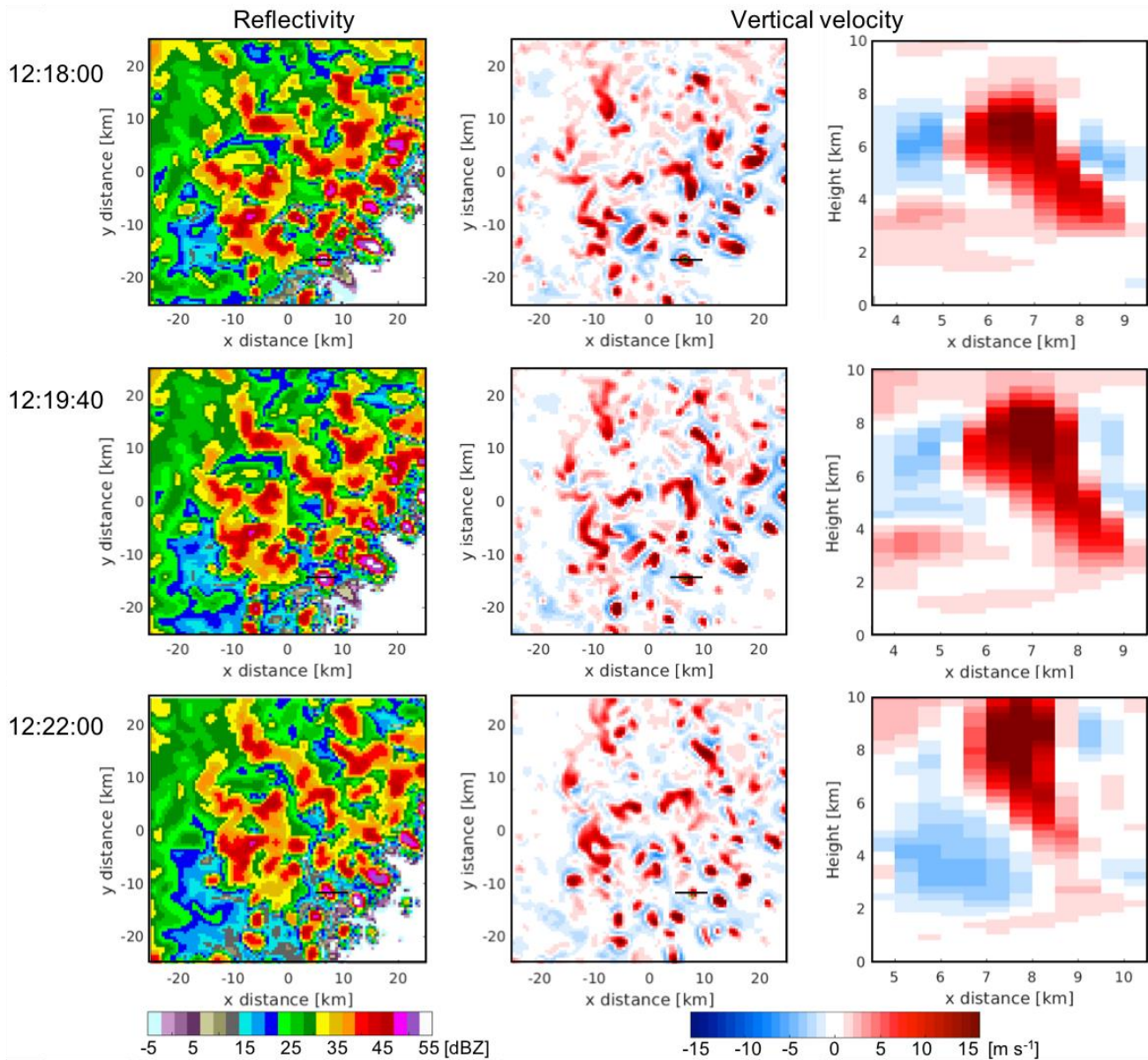
Figure 3: (Left column) Horizontal distributions of X-band *Z* at 7 km AGL from CR-SIM, (middle column) horizontal distributions of the WRF simulated vertical velocity at 7 km AGL, and (right column) vertical distributions of WRF-simulated vertical velocity along a line in the horizontal plots. Each row from top to bottom represents a simulation time of 12:18:00, 12:19:40, and 12:22:00 UTC, respectively.
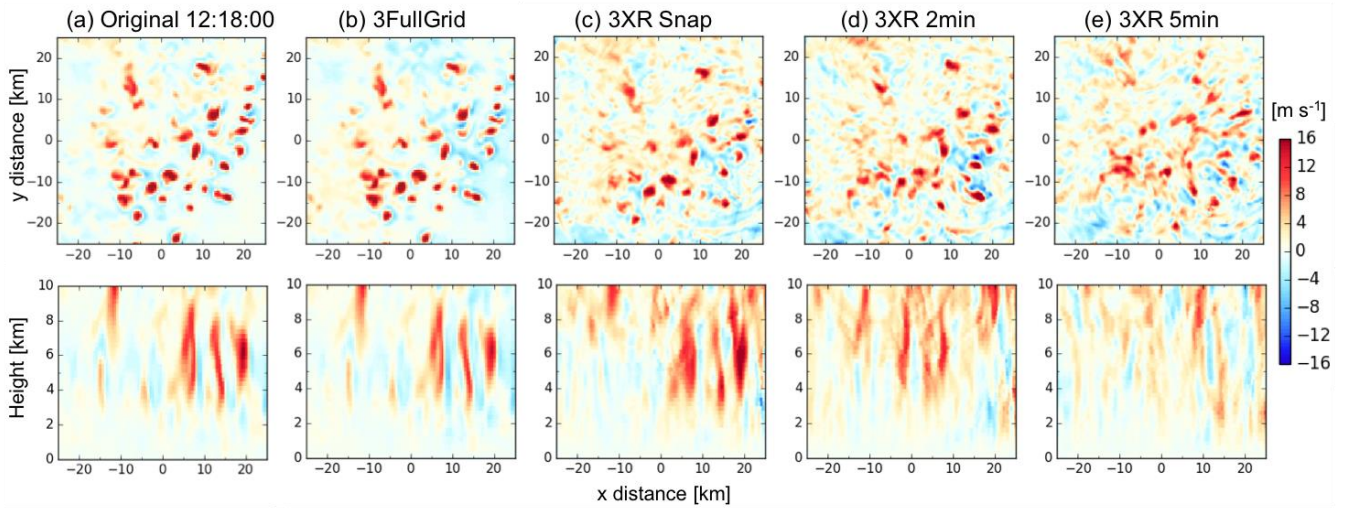
Figure 4: (Top row) Horizontal distributions at 7 km AGL and (bottom row) vertical cross sections at y = 0 km of vertical velocity. Each column represents (a) the original WRF vertical velocity field and the retrieved vertical velocity fields from the (b) 3FullGrid, (c) 3XRSnap, (d) 3XR2min, and (e) 3XR5min retrieval simulations.
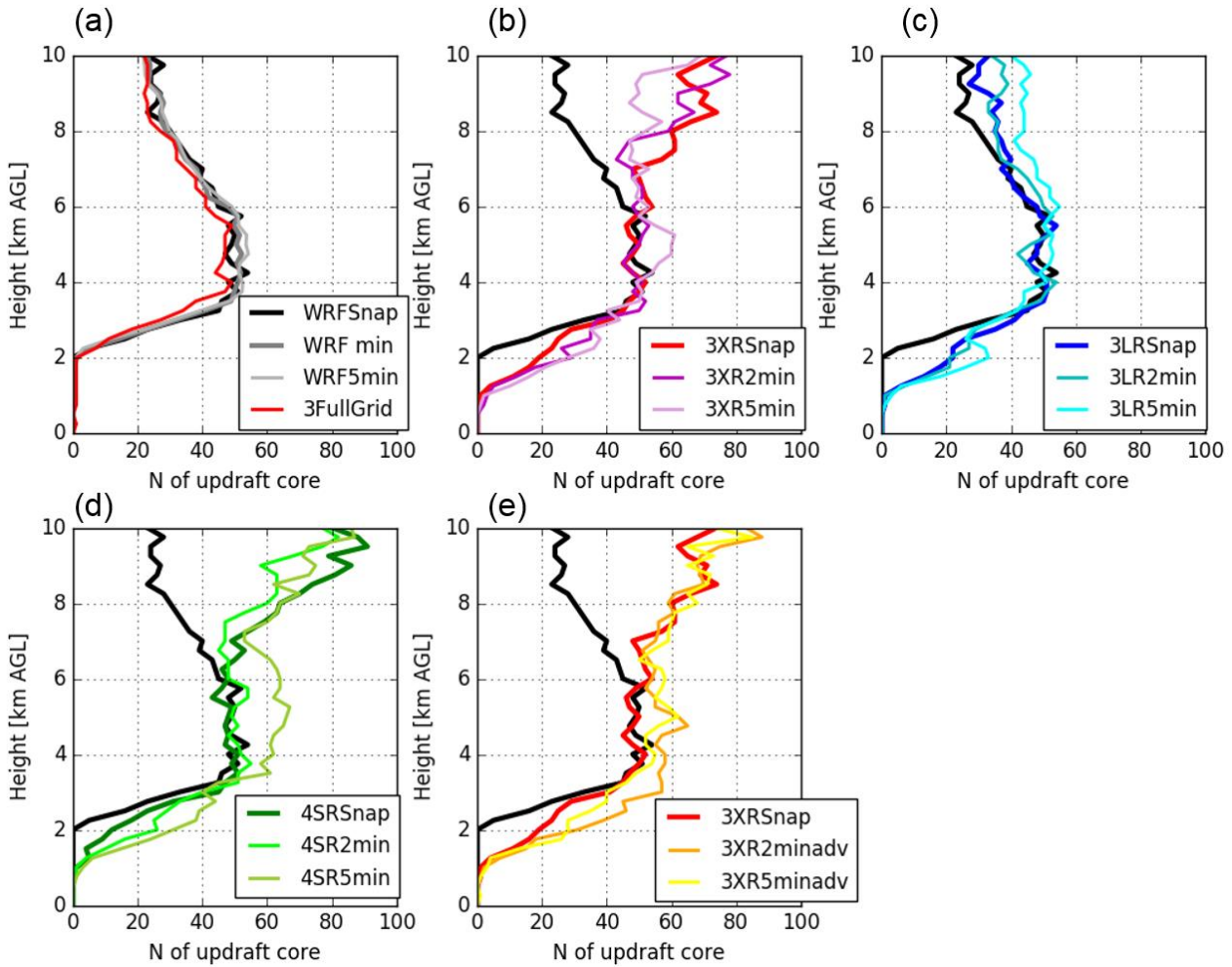
Figure 5: Vertical profiles of the number of coherent updrafts with vertical velocity > 5 m s⁻¹. Color represents different retrieval simulations as displayed in each panel. Dark gray line in (a) represents the WRF output averaged over 2 minutes from 12:18:00 to 12:19:40 UTC, and light gray in (a) represents the WRF output averaged over 5 min from 12:18:00 to 12:22:40 UTC. Each panel displays a profile from the WRF snapshot at 12:18:00 UTC by a black solid line.
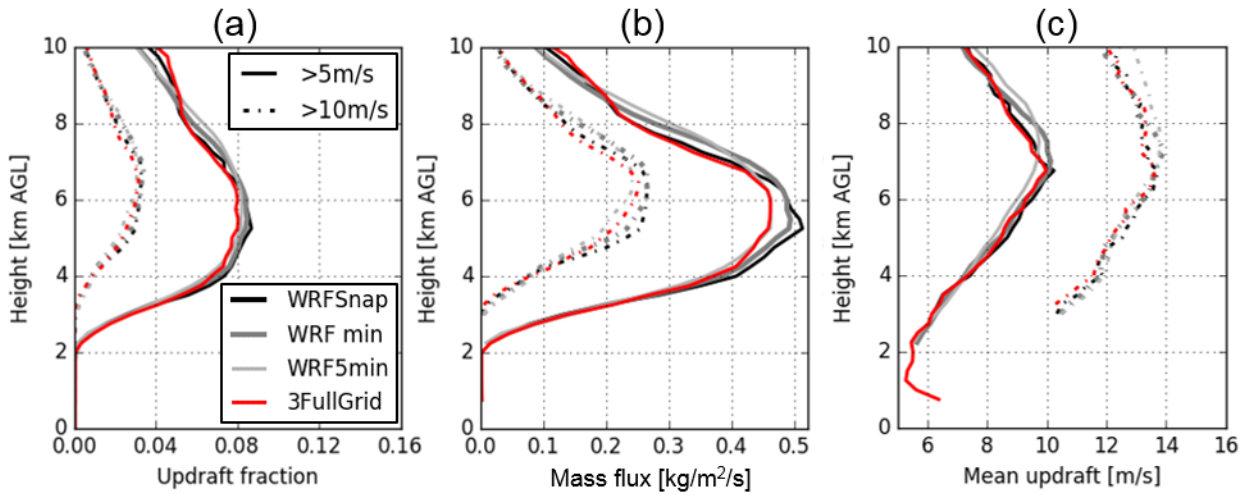
Figure 6: Vertical profiles of (a) updraft fraction, (b) mass flux, and (c) mean updraft velocity, with different thresholds of 5 m s⁻¹ (solid lines) and 10 m s⁻¹ (dashed lines) for the entire retrieval domain. Black lines represent the WRF snapshot at 12:18:00 UTC, dark gray lines represent the WRF output averaged over 2 minutes from 12:18:00 to 12:19:40 UTC, and light gray lines represent the WRF output averaged over 5 min from 12:18:00 to 12:22:40 UTC. Red lines represent the 3FullGrid retrieval simulation.
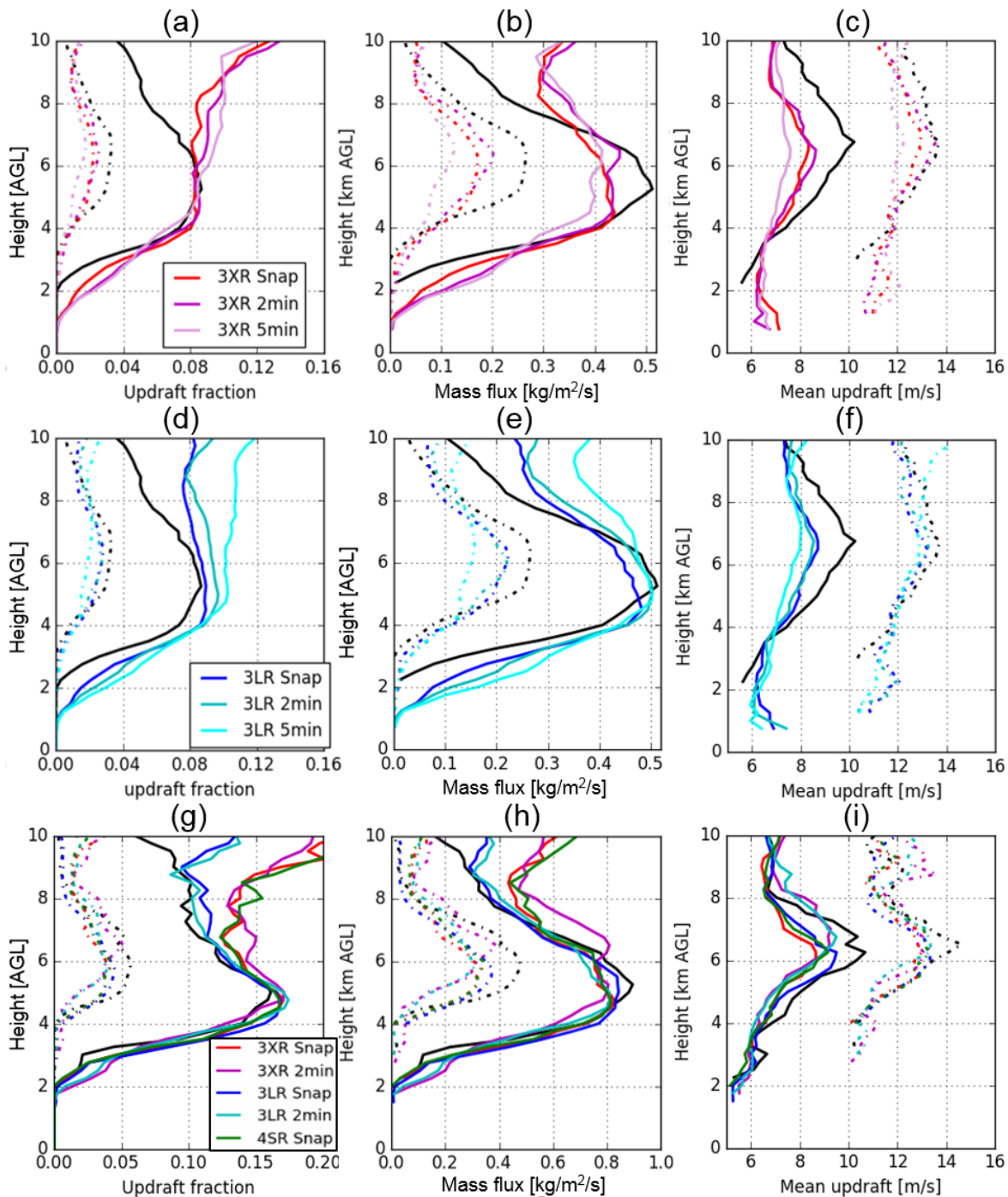
Figure 7: Vertical profiles of (left column) updraft fraction, (middle column) mass flux, and (right column) mean updraft velocity, with different thresholds of 5 m s^{-1} (solid lines) and 10 m s^{-1} (dashed

lines) for the entire retrieval domain (a – f) and a center region shown as a box in Fig. 2 (g – i). Color represents different retrieval simulations as displayed in panels in the left column. Each panel displays profiles from the WRF snapshot at 12:18:00 UTC by black lines.
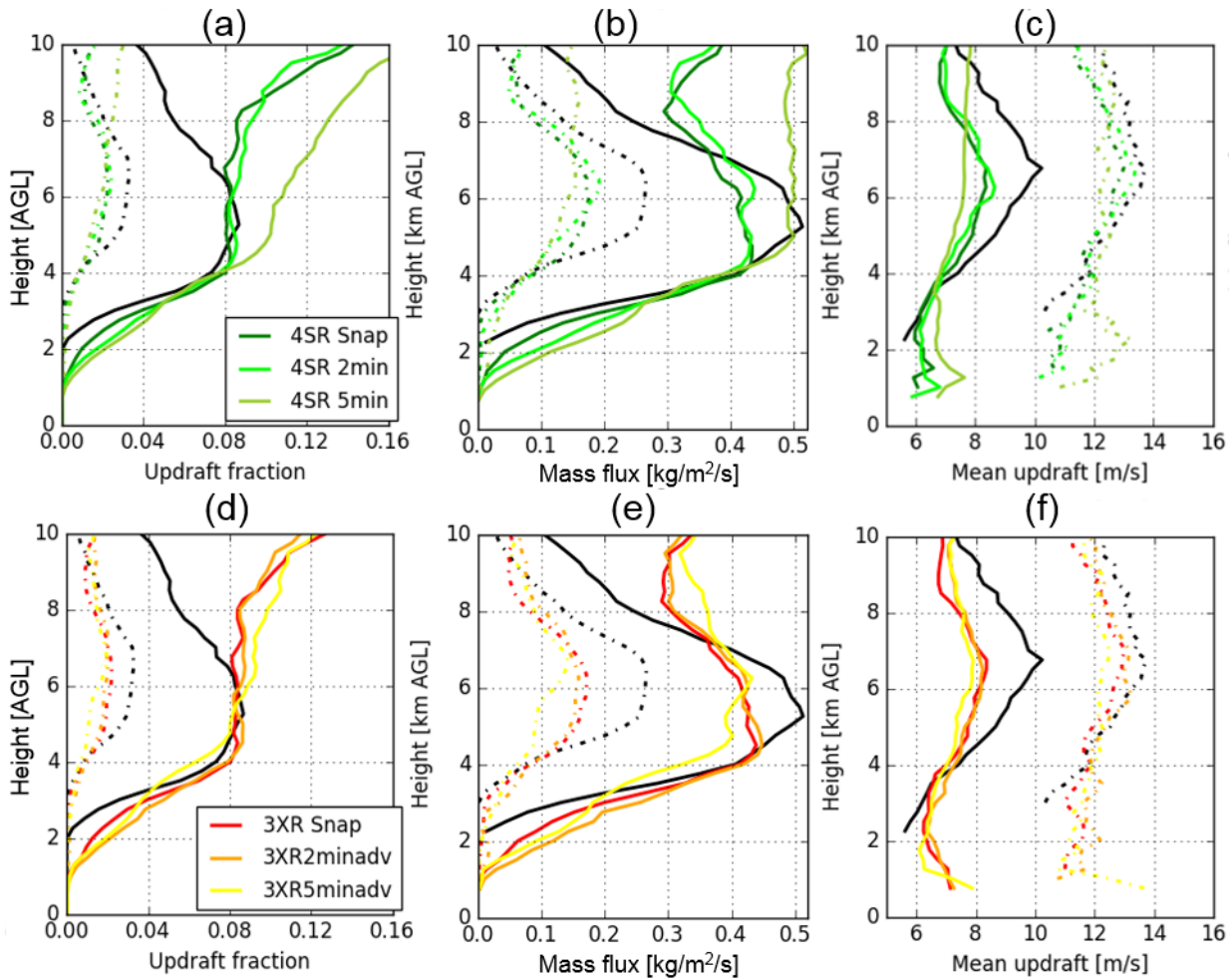
Figure 8: Vertical profiles of (left column) updraft fraction, (middle column) mass flux, and (right column) mean updraft velocity, with different thresholds of 5 m s^{-1} (solid lines) and 10 m s^{-1} (dashed lines) for the entire retrieval domain (a – f). Color represents different retrieval simulations as displayed in panels in the left column. Each panel displays profiles from the WRF snapshot at 12:18:00 UTC by black lines.
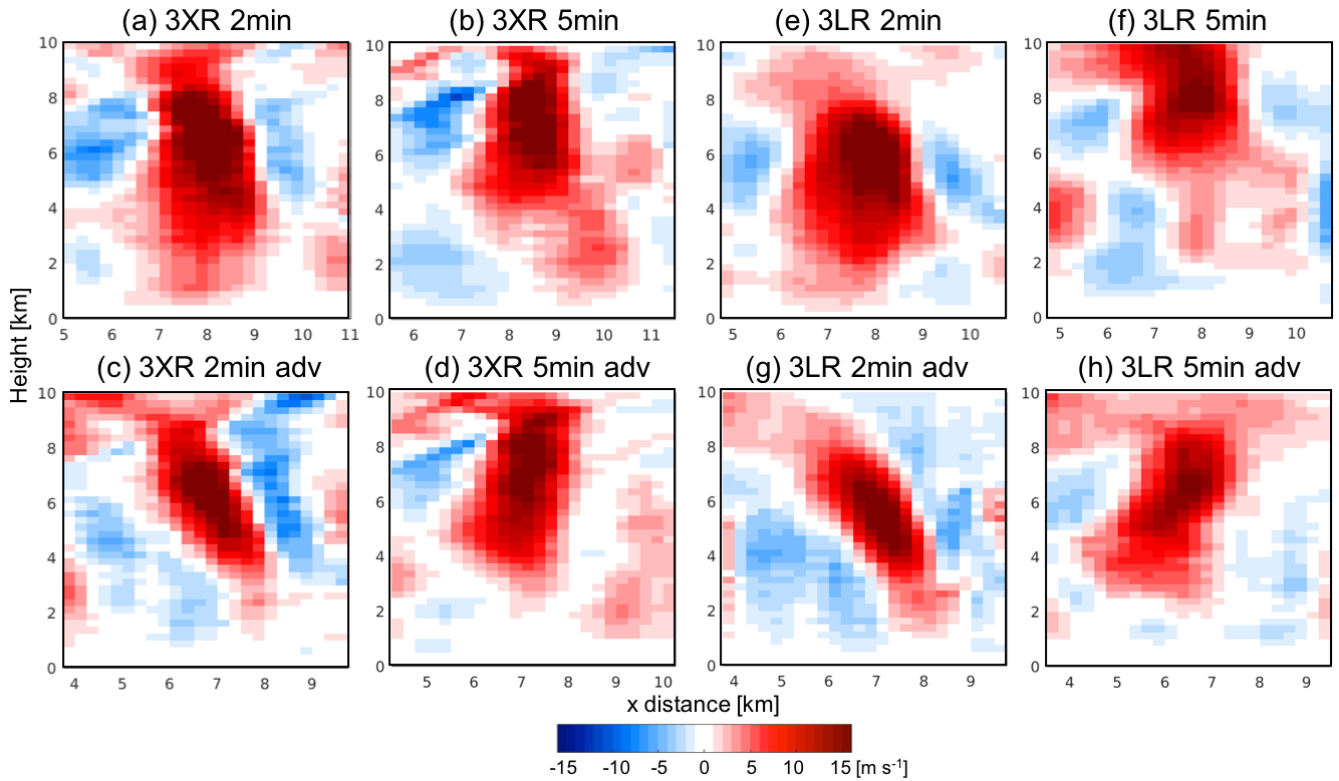
Figure 9: Vertical cross sections of vertical velocity for an updraft core from 3XR (a-d) and 3LR (e-h) wind retrieval simulations with 2-min and 5-min VCPs. Top raw and bottom raw display non-advection correction and advection-corrected retrievals, respectively. A selected updraft core is the same as shown in Fig. 3.